Technical Note: Constraining the hydroxyl (OH) radical in the tropics with satellite observations of its drivers: First steps toward assessing the feasibility of a global observation strategy

Daniel C. Anderson[1,2], Bryan N. Duncan[2], Julie M. Nicely[2,3], Junhua Liu[2,4], Sarah A. Strode[2,4], Melanie B. Follette-Cook[5]

1. GESTAR II, University of Maryland Baltimore County, Baltimore, MD, USA
2. Atmospheric Chemistry and Dynamics Laboratory, NASA Goddard Space Flight Center, Greenbelt, MD, USA
3. Earth System Science Interdisciplinary Center, University of Maryland, College Park, MD, USA
4. GESTAR II, Morgan State University, Baltimore, MD, USA
5. Mesoscale Atmospheric Processes Laboratory, NASA Goddard Space Flight Center, Greenbelt, MD, USA

Correspondence to: Daniel C. Anderson (daniel.c.anderson@nasa.gov)

Abstract

Despite its importance in controlling the abundance of methane (CH_4) and a myriad of other tropospheric species, the hydroxyl radical (OH) is poorly constrained due to its large spatial heterogeneity and the inability to measure tropospheric OH with satellites. Here, we present a methodology to infer tropospheric column OH (TCOH) in the tropics over the open oceans using a combination of a machine learning model, output from a simulation of the GEOS model, and satellite observations. Our overall goals are to assess the feasibility of our methodology, to identify potential limitations, and to suggest areas of improvement in the current observational network. The methodology reproduces the variability of TCOH from independent 3D model output and of observations from the Atmospheric Tomography mission (ATom). While the methodology also reproduces the magnitude of the 3D model validation set, the accuracy of the magnitude when applied to observations is uncertain because current observations are insufficient to fully evaluate the machine learning model. Despite large uncertainties in some of the satellite retrievals necessary to infer OH, particularly for NO_2 and HCHO, current satellite observations are of sufficient quality to apply the machine learning methodology, resulting in an error comparable to that of *in situ* OH observations. Finally, the methodology is not limited to a specific suite of satellite retrievals. Comparison of TCOH determined from two sets of retrievals does show, however, that systematic biases in NO_2, resulting both from retrieval algorithm and instrumental differences, lead to relative biases in the calculated TCOH. Further evaluation of NO_2 retrievals in the remote atmosphere is needed to determine their accuracy. With slight modifications, a similar methodology could likely be expanded to the extra-tropics and over land, with the benefits of increasing our understanding of the atmospheric oxidation capacity and, for instance, informing understanding of recent CH_4 trends.

1   Introduction

The hydroxyl radical (OH) dictates the lifetime of many tropospheric species, including carbon monoxide (CO), methane (CH_4), and numerous volatile organic compounds (VOCs). Knowledge of OH is therefore necessary to understand the abundance, distribution, and variability of these species. For instance, Rigby et al. (2017) and Laughner et al. (2021) attribute recent trends and increases in CH_4 at least partially to changes in OH abundance. Current constraints on OH are insufficient, however, to assess its relative importance in controlling these trends (Turner et al., 2017).

48   Differences in OH distributions among chemistry transport (CTM) and chemistry climate models (CCM)
49   suggest that these models are insufficient to inform understanding of OH abundance and variability
50   without further observational constraints. OH abundance can differ by up to 80% among models
51   constrained with identical emissions in intercomparison projects (Voulgarakis et al., 2013;Nicely et
52   al.;Zhao et al., 2019;Murray et al., 2021), with modeled trends disagreeing with those derived from
53   observationally constrained methods (Stevenson et al., 2020). Variables such as the photolysis
54   frequency of O_3 (JO^1D) (Nicely et al., 2020), the NO_X lifetime ($NO_X = NO + NO_2$), and the oxidation
55   efficiency of VOCs (Murray et al., 2021) contribute to these inter-model variations in OH. Using
56   Gaussian emulation, Wild et al. (2020) found that the relative importance of drivers of OH variability
57   differed widely among three CTMs. Likewise, the response of OH to the El Niño Southern Oscillation
58   (ENSO), the dominant mode of OH variability on monthly and seasonal timescales (e.g. Anderson et al.,
59   2021;Turner et al., 2018), and other modes of internal climate variability can vary widely among models
60   (Anderson et al., 2021).
61
62   Despite this need for better constraints, observations of tropospheric OH are limited. The hydroxyl
63   radical has a lifetime of approximately 1s (Mao et al., 2009), resulting in large spatial heterogeneity in
64   both the horizontal and vertical. This spatial heterogeneity is further caused by the large variation in the
65   relative importance of drivers of OH loss and production in different regions of the atmosphere (e.g.
66   Spivakovsky et al., 1990;Lelieveld et al., 2016). A strategic, representative in situ observational network
67   is therefore unfeasible. As a result, observations of OH are generally limited to intensive field campaigns
68   (Miller and Brune, 2022) that have narrow spatial and temporal coverage. While remotely-sensed OH
69   observations are available, those from satellites are limited to the stratosphere (e.g., Pickett et al.,
70   2008), while ground-based observations of total column OH are dominated by the stratospheric
71   contribution (e.g., Burnett and Minschwaner, 1998).
72
73   Reference gases with well-characterized sources and an OH sink, such as methyl chloroform (MCF), can
74   be used to infer OH abundance (Lovelock, 1977). This methodology, however, generally yields no
75   information on spatial heterogeneity beyond the hemispheric scale (e.g., Montzka et al., 2011;Rigby et
76   al., 2017;Naus et al., 2019), although there has been recent success when using three dimensional
77   inversion techniques (Naus et al., 2021) For MCF in particular, recent declines in tropospheric
78   abundance will soon dictate the need for a new reference species (Liang et al., 2017).
79
80   Multiple studies have attempted to constrain OH through the creation of proxies and the application of
81   satellite retrievals of OH drivers. Murray et al. (2014) showed that global OH strongly correlated with a
82   combination of JO^1D, water vapor ($H_2O_{(v)}$), and the tropospheric sources of reactive nitrogen and carbon
83   in the GEOS-Chem model. Murray et al. (2021) demonstrated that OH correlated with this proxy in
84   multiple CTMs, although the relationship differs strongly among models. Miyazaki et al. (2020) created
85   a data assimilation framework that ingested satellite observations of CO, NO_2, O_3, and HNO_3 (nitric acid)
86   into multiple CTMs. The data assimilation reduced the spread in average OH among the models and
87   brought the interhemispheric ratio closer to unity, in line with values suggested by MCF observations
88   (e.g. Patra et al., 2014). These results demonstrate that the incorporation of satellite observations into a
89   modeling framework can improve the representation of OH. Wolfe et al. (2019) developed a proxy for
90   OH based on formaldehyde (HCHO) production and loss rates. They applied that proxy to satellite HCHO
91   observations to estimate OH columns in the remote troposphere, a region where HCHO abundance is
92   low and the satellite retrievals are reflective of the *a priori* (Zhu et al., 2016). Using machine learning,
93   chemical transport model output, and retrievals of NO_2 and HCHO, Zhu et al. (2022b) developed a
94   method to estimate surface OH in North American urban areas. Finally, Pimlott et al. (2022) used a
95   steady state approximation of OH, including primary production from H_2O and O_3 and loss from CO, CH_4,

96   and O_3, to estimate OH between 600 and 700 hPa using observations from IASI (Infrared Atmospheric
97   Sounding Interferometer). A logical next step, building on the results of these studies, is the
98   development of a methodology to constrain OH that ingests multiple satellite retrievals, encompasses
99   the breadth of OH chemical and dynamical drivers, and spans a significant enough portion of the globe
100 to inform variability and trends in CH_4 and CO loss.
101
102 Combining machine learning, chemical transport model (CTM) output, and satellite data has the
103 potential to constrain tropospheric column OH (TCOH). A variety of machine learning techniques, such
104 as neural networks (Nicely et al., 2017;Nicely et al., 2020;Kelp et al., 2020), self-organizing maps
105 (Stauffer et al., 2016), random forest regression (Keller and Evans, 2019), and gradient boosted
106 regression trees (GBRTs) (Ivatt and Evans, 2020;Zhu et al., 2022b;Anderson et al., 2022) show promise in
107 helping to solve problems in atmospheric chemistry. In particular, Zhu et al. (2022b) and Anderson et al.
108 (2022) demonstrated the ability of GBRTs to predict OH from a chemical transport model with
109 reasonable accuracy. GBRT models (Elith et al., 2008;Chen and Guestrin, 2016) use an ensemble of
110 decision trees to predict the value of a target based on multiple inputs, even for targets with highly non-
111 linear dependencies on the inputs.
112
113 Here, we present a methodology to infer clear sky TCOH in the tropics from space-based observations of
114 its chemical and dynamical drivers with the goal of assessing the feasibility of our methodology,
115 identifying potential limitations, and suggesting areas of improvement in the current observational
116 network. We train a GBRT model using output from a simulation of the NASA GEOS (Goddard Earth
117 Observing System) model, and then estimate TCOH in the actual atmosphere at the satellite overpass
118 time using inputs from a suite of satellite retrievals. In Section 2, we describe the methodology for
119 generating the machine learning model as well as the satellite retrievals used to constrain TCOH. We
120 then evaluate the suitability of MERRA2 GMI as a training dataset (Sect. 3) and, in Section 4, present a
121 satellite-constrained OH product for one month from each season. Finally, in Section 5, we explore
122 potential methodological limitations and benefits, including lack of validation data, the impacts of
123 observational uncertainties, and the ability to use different satellites and retrievals as inputs to the GBRT
124 model.
125
126 **2   Description of the methodology to generate the GBRT model and of the associated datasets**
127 Our overall aim is to demonstrate the feasibility of our approach to constrain TCOH with satellite-based
128 observations over broad regional scales. As a first step, we restrict our analysis to latitudes equatorward
129 of $25°$ and regions over water. We chose to focus initially on this domain as it has appreciable OH
130 concentrations and simplified chemistry, as compared to regions with large biogenic and anthropogenic
131 VOC emissions. Nevertheless, this portion of the atmosphere accounts for $50 - 60\%$ of global CO and
132 CH_4 loss. In this section, we describe the creation of the machine learning model used to predict TCOH
133 (Sect. 2.1) for this region as well as the satellite products used as inputs to the machine learning model
134 (Sect. 2.2).
135
136 **2.1 Creation of the TCOH model**
137 **2.1.1 Creation of the GBRT training dataset**
138 For the machine learning model training dataset, we use a subset of output from the MERRA2 GMI
139 simulation (https://acd-ext.gsfc.nasa.gov/Projects/GEOSCCM/MERRA2GMI/). MERRA2 GMI is a 40 year
140 (1980 – 2019) simulation of the NASA GEOS model run in replay mode (Orbe et al., 2017) with MERRA2
141 (Modern Era Retrospective analysis for Research and Applications, version 2) meteorology (Gelaro et al.,
142 2017). The simulation has a resolution of c180 on the cubed sphere (approximately $0.625°$ longitude by
143 $0.5°$ latitude) with 72 vertical layers and uses the Global Modeling Initiative (GMI) chemical mechanism

144   (Duncan et al., 2007;Strahan et al., 2007). Output is available at daily- and monthly-averaged resolution,
145   as well as instantaneous values at 10:00 and 14:00 LST. These times are within approximately 30
146   minutes of the overpass times of the satellites described in Section 2.2. Anderson et al. (2021) and
147   Strode et al. (2019) provide detailed information about the simulation, including emissions.
148
149   The training target for the machine learning model is TCOH. In Anderson et al. (2022), we developed a
150   GBRT parameterization trained on MERRA2 GMI output to predict in situ OH concentrations using 27
151   inputs, only a small fraction of which are observable from space. That parameterization, designed to be
152   integrated into the GEOS modeling framework, performed better when there was a separate model for
153   each month as opposed to one model for all months. While that GBRT model is not appropriate for the
154   application described here, we employ a similar approach, creating a separate set of TCOH training
155   targets for each month. We use instantaneous OH output from MERRA2 GMI at 14:00 local time for
156   each day of a given month across the years 2005 to 2019, a timeframe that maximizes overlap between
157   the operational lifetime of the satellites listed in Table 1 and the period of the MERRA2 GMI simulation.
158   We omitted data from 2017 to evaluate model performance. For a given month and year, we calculate
159   daily tropospheric column values across the grid, filtering out columns where the maximum cloud
160   fraction in that column was greater than 30% in order to align the training targets more closely with
161   satellite data, where retrievals of some species are often filtered for cloud cover. This yields
162   approximately 43,000 valid grid boxes per day. For each year, we then average these values to monthly
163   resolution. This results in approximately 600,000 total training targets for each month over the 15-year
164   period.
165
166   ***Table 1***: Input variables to the machine learning model and the corresponding satellite retrieval used to create the
167   satellite OH product. Overpass times are ~13:30 LST for all satellites except MOPITT, which has a 10:30 LST
168   overpass.

Variable	Satellite retrieval	Original horizontal and temporal resolution	Reference
Total O_3 column	OMI TOMS-Like L3 version 3	$0.25° \times 0.25°$, daily	McPeters et al. (2015)
Tropospheric NO_2 column	OMI GSFC L3 version 4	$0.25° \times 0.25°$, daily	Lamsal et al. (2021)
CO column	MOPITT L3 version 8	$1.0° \times 1.0°$, monthly	Deeter et al. (2019)
HCHO column	OMI SAO L3 version 3	$0.1° \times 0.1°$, daily	González Abad et al. (2015)
$H_2O_{(v)}$ column	AIRS L3 version 6	$1.0° \times 1.0°$, monthly	Susskind et al. (2014)
Sea surface temperature	MUR L4 version 4.2	$0.25° \times 0.25°$, daily	Chin et al. (2017)
Aerosol optical depth at 550 nm	MODIS Aqua L3 collection 6	$0.5° \times 0.5°$, daily	Levy et al. (2013)
$H_2O_{(v)}$ layers: $925 - 850$ hPa, $850 - 700$ hPa, $700 - 600$ hPa, $600 - 500$ hPa, $500 - 400$ hPa, $400 - 300$ hPa, and 300 - 250 hPa	AIRS L3 version 6	$1.0° \times 1.0°$, monthly	Susskind et al. (2014)
Solar zenith angle	N/A		
Latitude	N/A		

169
170   We selected the input variables for the machine learning model (Table 1) based on their relevance to OH
171   chemistry and variability as well as our current ability to observe the variable with satellites.
172   Performance was similar for a model including total column ozone only and for a model also including
173   the tropospheric column. We therefore use total column ozone because of the uncertainties inherent in

174 separating the column into two parts in the satellite retrieval. We chose the water vapor layers to
175 correspond with the Atmospheric Infrared Sounder (AIRS) layers product. Layers are averages over the
176 indicated pressure range, and we denote the layer names by the highest pressure in that range. We
177 include sea surface temperatures (SST) as a proxy for the Indian Ocean Dipole and ENSO, which has a
178 strong impact on OH variability in the tropics (Anderson et al., 2021;Turner et al., 2018;Naus et al.,
179 2021). In addition, we include latitude and solar zenith angle as previous work has shown that these
180 variables can explain a large fraction of the spatial OH variability (Duncan et al., 2000;Anderson et al.,
181 2022).

182
183 We sampled the MERRA2 GMI output to create the training dataset in the same manner as for the TCOH
184 targets. The inputs to the machine learning model each correspond to the same model column as the
185 OH target. All column values are instantaneous and taken from 14:00 to correspond with satellite
186 overpass times, except for CO, which is for 10:00, near the Measurement of Pollution in the
187 Troposphere (MOPITT) overpass time. Model performance was similar when using CO output at 14:00
188 and 10:00, likely because of limited diurnal variability in CO column in the study region. SSTs are
189 monthly averages of 24-hour averaged values, and we calculated solar zenith angle at the surface for
190 noon on the 15th of a given month.

191
192 **2.1.2 Creation and tuning of the GBRT model**
193 We used the XGBoost package (Chen and Guestrin, 2016) version 0.81 in Python version 3.6 to create a
194 GBRT model of TCOH for each month using the training datasets from MERRA2 GMI. For each month,
195 we used 90% of the dataset for model training and the remainder for model validation. As mentioned in
196 Section 2.1.1, we also used MERRA2 GMI output from 2017, which was omitted from the training
197 dataset, as further validation.

198
199 To maximize parameterization performance while also balancing the potential of overfitting, we tuned
200 hyperparameters, including the learning rate, the maximum tree depth, and the number of trees. We
201 chose hyperparameter values that minimized the parameterization root mean square error (RMSE) of
202 the training dataset. We set the learning rate, which controls the magnitude of change when adding a
203 new tree, to 0.1, while we varied the maximum tree depth and number of trees from 6 to 22 and from
204 10 to 150, respectively. For both maximum tree depth and number of trees, RMSE initially dropped
205 significantly with increasing value, representing sharp improvement in parameterization performance.
206 RMSE values eventually plateaued, increasing parameterization runtime without noticeably improving
207 performance. A combination of a maximum tree depth of 18 and 100 trees balanced performance with
208 model training and run time.

209
210 To determine whether the inputs to the machine learning model improved or hindered performance, we
211 performed a "leave one out" analysis. Using 5-fold cross validation, we retrained the model, individually
212 omitting each of the inputs, to determine the percent difference between the mean RMSE of the 5 folds
213 for the model without a specific input and one including all inputs. Omitting the inputs listed in Table 1
214 lead to increases in the RMSE, suggesting that each is necessary for improved model performance. As a
215 result of this analysis, we do not use water vapor layers for pressures less than 300 hPa because these
216 decreased model performance.

217
218 Finally, we found that it was not necessary to apply satellite averaging kernels and shape factors to the
219 training dataset. Of the satellite retrievals used in this work (discussed in Sect. 2.2 and listed in Table 1),
220 only CO, HCHO, and NO$_2$ could require convolving the model with the averaging kernel. Shape factors
221 for the OMI NO$_2$ retrieval are determined from a similar setup of the GEOS model, also employing the

222   GMI chemical mechanism and MERRA2 meteorology. Applying the satellite shape factors to the
223   simulation discussed here would therefore not result in significant changes in the modeled NO_2
224   (Anderson et al., 2021). To test whether it is necessary to apply the averaging kernels for CO and HCHO,
225   we created a separate training dataset, where we convolved the daily MERRA2 GMI output with the
226   averaging kernel and a priori from the level 2 data for both species for February 2005 - 2019. All other
227   inputs were kept the same. We then retrained the model with these adjusted CO and HCHO variables.
228   When we applied the satellite data to the model for February 2017, as described in Section 4, the
229   resulting TCOH differed by less than 1% on average from the model that did not include averaging kernel
230   information. This level of uncertainty is significantly smaller than the other uncertainties discussed in
231   Section 5, so we do not include averaging kernels in our analysis.
232
233   **2.2 Description of satellite products**
234   To create the observationally-constrained OH product, we use multiple satellite retrievals, listed in Table
235   1 and briefly described here. Each instrument is located onboard a polar orbiting satellite that provides
236   near global coverage daily. For each satellite retrieval, we use the level 3 gridded product, with the
237   exception of SST which is level 4. Where necessary, we regridded the retrieval to a common horizontal
238   grid with a resolution of $1.0° \times 1.0°$ and averaged to the monthly scale.
239
240   We use these resolutions because, in the study domain, individual pixel retrievals, particularly of NO_2
241   and HCHO, are frequently at or below detection limits (González Abad et al., 2015;Lamsal et al., 2021),
242   necessitating averaging to relatively coarse temporal and spatial scales. Missing data due to cloud cover
243   and the Ozone Monitoring Instrument (OMI) row anomaly further increase the need for monthly-scale
244   averaging. While other satellites, such as OMPS (Ozone Mapping and Profiler Suite) and TROPOMI
245   (Tropospheric Monitoring Instrument), provide retrievals with increased signal to noise ratios and more
246   complete data coverage, the satellites used here cover a far longer time period. The $1.0° \times 1.0°$ and
247   monthly resolutions, in combination with the long data record, are sufficient to understand regional
248   trends in TCOH and some aspects of TCOH temporal and spatial variability.
249
250   We use retrievals of three species – HCHO, O_3, and NO_2 – from OMI, an ultraviolet-visible spectrometer
251   located onboard the Aura satellite, which has an overpass of approximately 13:30 local solar time (LST).
252   We use the Smithsonian Astrophysical Observatory (SAO) version 3 HCHO retrieval (González Abad et
253   al., 2015). Wolfe et al. (2019) found that this retrieval captured the variability of the HCHO columns in
254   the remote atmosphere observed during the Atmospheric Tomography (ATom) campaign with little bias.
255   For total column O_3, we use the TOMS-like (Total Ozone Mapping Spectrometer) retrieval version 3
256   (McPeters et al., 2015), which agrees with ground-based and other satellite observations within
257   approximately 1% (Labow et al., 2013). Finally, we use the Goddard Space Flight Center version 4 NO_2
258   tropospheric column retrieval (Lamsal et al., 2021). While previous studies have thoroughly evaluated
259   this retrieval in more polluted atmospheres (e.g., Lamsal et al., 2014;Choi et al., 2020), evaluation in the
260   remote tropical atmosphere, as defined in this study, is limited.
261
262   For water vapor and aerosol optical depth (AOD) at 550 nm, we use retrievals from AIRS and the
263   Moderate Resolution Imaging Spectroradiometer (MODIS) instruments, respectively, both located
264   onboard the Aqua satellite with an overpass of approximately 13:30 LST. We use the total column water
265   vapor standard physical retrieval as well as the 7 water vapor layers listed in Table 1 (Susskind et al.,
266   2014). Multiple studies have evaluated the accuracy of the AIRS $H_2O_{(v)}$ column and layers retrievals in
267   the remote tropical atmosphere, finding bias of 5% or less and high correlation against both remote and
268   *in situ* observations (Bedka et al., 2010;Anderson et al., 2016;Pérez-Ramírez et al., 2019). We use

269 collection 6 of the dark target MODIS AOD retrieval at 550 nm, which is highly correlated with
270 observations from the AERONET network over the ocean (Levy et al., 2013).
271
272 We also use retrievals of CO from MOPITT, which is onboard the Terra satellite with an overpass of
273 10:30 LST. We use the version 8 retrieval that includes both near and thermal infrared radiances (Deeter
274 et al., 2019). CO retrievals from MOPITT in the remote tropics generally agree with ground-based
275 remotely-sensed observations within 10% (Hedelius et al., 2019;Buchholz et al., 2017).
276
277 Finally, we use SSTs from the Multi-scale Ultra-high Resolution (MUR) analysis, which combines
278 nighttime SST observations from multiple satellite platforms, including MODIS, as well as *in situ*
279 observations and agrees with other SST analyses within 0.36° C (Chin et al., 2017).
280
281 **3   Evaluating the Suitability of the MERRA2 GMI Simulation as a Training Dataset**
282 Before generating the GBRT model to predict TCOH, we first demonstrate that the MERRA2 GMI
283 simulation is suitable to use as a training dataset. Because of the paucity of in situ observations of OH
284 over most of the globe, we necessarily use output from an atmospheric chemistry model to train the
285 machine learning model. The atmospheric chemistry model output must reasonably capture the
286 distribution, magnitude, and ENSO-related variability of OH and the drivers listed in Table 1, as GBRT
287 models are unable to extrapolate beyond the photochemical environments on which they are trained
288 (Anderson et al., 2022).
289
290 **3.1 Comparison of the Distribution and Magnitude of Simulated OH Drivers to Observations**
291 Simulated OH from MERRA2 GMI agrees with observations over the remote ocean within the
292 instrumental uncertainty. Anderson et al. (2021) compared MERRA2 GMI output to in situ observations
293 from the first two deployments of ATom, finding modest correlation (r^2 values between 0.3 and 0.78
294 depending on the hemisphere and season) between observations and the model. The average
295 normalized mean bias was on the order of 20%, a slight high bias but within the 2σ observational
296 uncertainty of 35%. Agreement was highest in the remote atmosphere, whereas the largest error was in
297 regions of fresh, continental outflow off the coasts of South America and New Zealand.
298
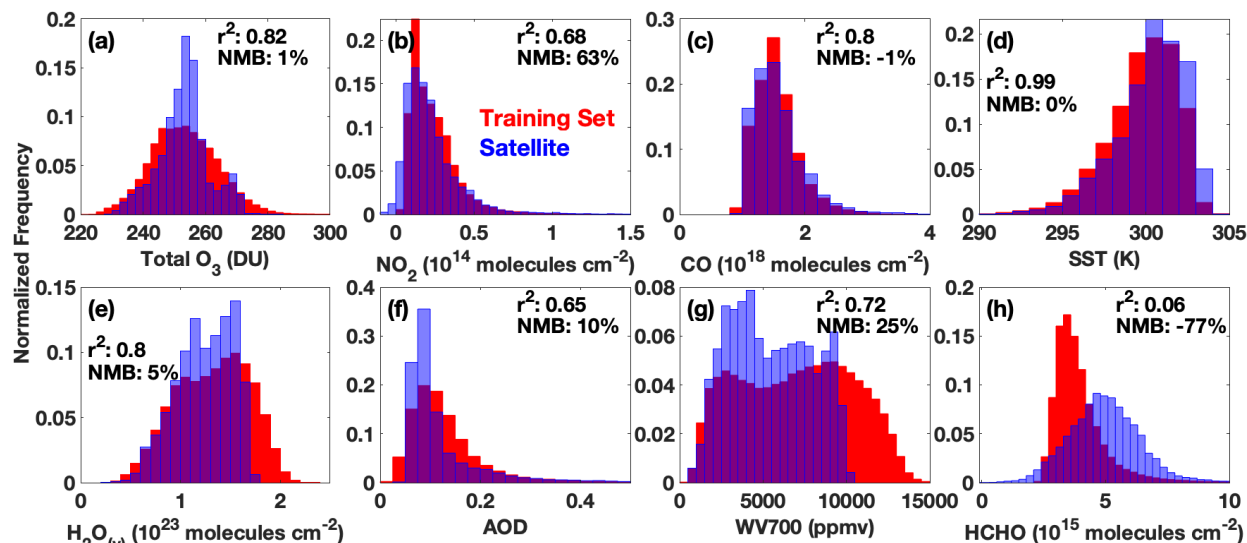
300 **Figure 1:** Comparison of the normalized distributions of the training dataset (red) for the February model and
301 satellite observations of the indicated species for February 2017 (blue). Purple indicates regions of overlap. We

302   use $H_2O_{(v)}$ at 700 hPa as an example for all $H_2O_{(v)}$ layers. Distributions of the other $H_2O_{(v)}$ layers are shown in Figure
303   S1. We also indicate the r^2 of the correlation between MERRA2 GMI output for February 2017 and the
304   corresponding satellite retrieval as well as the normalized mean bias of that output.

305   The simulation captures both the observed variability and the magnitude of the majority of GBRT model
306   inputs with reasonable fidelity, suggesting that the satellite retrievals highlighted in Section 2.2 are
307   suitable inputs for a machine learning model trained on MERRA2 GMI output (Fig.1). Figure 1 compares
308   the distribution of the February training dataset created from the MERRA2 GMI simulation for 2005 –
309   2019 to the satellite observations of the indicated species for February 2017, a month omitted from the
310   training dataset. Distributions of the remaining water vapor layers are shown in Figure S1. In addition,
311   correlations between observations and MERRA2 GMI output for February 2017 are shown, as an
312   example, in Figures S2 and S3. With the exception of HCHO, distributions of the species are similar
313   between the observations and MERRA2 GMI, with the training dataset encompassing the full range of
314   almost all species. A GBRT model trained on MERRA2 GMI will therefore likely not have to extrapolate
315   to photochemical environments on which it was not trained when applied to the satellite data. Further,
316   MERRA2 GMI total column O_3, $H_2O_{(v)}$ column, AOD, CO, and SSTs are all highly correlated (r^2 of 0.65 or
317   higher) with their respective satellite observations, and biases are within 10%, on average. Anderson et
318   al. (2021) did show that MERRA2 GMI CO columns demonstrate biases of opposite sign in the Northern
319   and Southern Hemispheres, however.
320
321   Agreement between MERRA2 GMI and satellite observations for NO_2, HCHO, and the $H_2O_{(v)}$ layers is
322   more variable than for the other species. While modeled NO_2 is moderately correlated with
323   observations (r^2 = 0.68) with relatively similar distributions, MERRA2 GMI has a NMB of 63%. This
324   disagreement is most pronounced at low column values, however, where observational uncertainty is
325   large. Further, Anderson et al. (2021) demonstrated distinct regions of bias in NO_2 related to biomass
326   burning and lightning emissions. Modeled HCHO, on the other hand, is not correlated with observations
327   and is biased low by -77%. Modeled water vapor layers are all modestly correlated with observations (r^2
328   of 0.64 or greater) but vary in their bias, with the 925, 850, 700, and 300 hPa layers biased within 30%
329   and the remaining layers biased up to 71%.
330
331   The satellite product is insensitive to the differences between the HCHO distribution of the satellite and
332   training dataset highlighted in Figure 1. To determine the effects of the difference in HCHO distribution,
333   we extended the training dataset to cover the full time period of the MERRA2 GMI simulation (1980 –
334   2019) and then subsampled the resultant data to match the satellite HCHO distribution. Extending the
335   training dataset to 1980 allows for the subsampled training dataset to have a similar size (~600,000
336   points) as the original training set. We then created a new machine learning model using this sub-
337   sampled dataset and calculated OH fields for Feb. 2017 using the satellite inputs from Table 1. We
338   compared this to the TCOH field calculated from a model using the original training dataset, finding
339   agreement within 5%. Similarly, the satellite-constrained TCOH product discussed in Section 4.2 differs
340   by only 3% on average from one determined with a GBRT model that excludes HCHO as an input,
341   suggesting the limited impact of potential errors in the MERRA2 GMI HCHO distribution on model
342   performance. These uncertainties are small in comparison to that resulting from uncertainties in the
343   NO_2 and HCHO satellite retrievals discussed in Section 5.2. If the uncertainty of the satellite inputs
344   decreases, as retrievals and instruments improve, then it will become necessary to more closely align
345   the training and observed HCHO distributions.
346
347   Finally, because NO_2 and HCHO have the largest differences between satellite observations and the
348   training dataset, we trained a separate machine learning model to predict TCOH, omitting these two

8

349 species as inputs. When this model was evaluated using the independent MERRA2 GMI output
350 described in Section 4.1, the NRMSE was 10.1%, a more than factor of 2 degradation in performance as
351 compared to the baseline model. This suggests that omitting these species from the machine learning
352 model would result in a greater uncertainty in the final TCOH product than that which results from the
353 retrieval uncertainties and the potential discrepancies between observations and the training dataset.
354
355 **3.2 Evaluation of the simulated ENSO-related variability of OH drivers**
356 Because ENSO is the dominant mode of OH variability (Anderson et al., 2021;Turner et al., 2018), the
357 training dataset must also capture the ENSO-related variability of the GBRT model inputs. Anderson et
358 al. (2021) demonstrated that the correlation of columns of CO, $H_2O_{(v)}$, and to a lesser extent NO_2, from
359 the MERRA2 GMI simulation with the Multivariate ENSO Index (MEI) (Wolter and Timlin, 2011) agreed
360 closely with correlations of the corresponding species for observations from MOPITT, AIRS, and OMI.
361 Unsurprisingly, based on the strong correlation and low bias of MERRA2 GMI SSTs with observations, the
362 simulation also captures the relationship between SSTs and ENSO. The simulation therefore sufficiently
363 captures the ENSO-related variability of these species to act as training data for the GBRT model. We
364 now evaluate this relationship for the remaining GBRT model inputs.
365
366 The MERRA2 GMI-simulated ENSO-related variability of AOD and the various water vapor layers also
367 agrees well with observations. Figures 2 and S4 show the correlation of AOD, HCHO, and the various
368 $H_2O_{(v)}$ layers with the MEI for the satellite retrievals and MERRA2 GMI. MERRA2 GMI captures the
369 general distribution and magnitude of correlation between AOD and ENSO, despite the low optical
370 depths over much of the domain. There are some regional differences, however, particularly in the
371 eastern Southern Hemispheric Pacific. For the $H_2O_{(v)}$ layers, the simulation underestimates the
372 magnitude of the correlation in some areas, but in general, there is excellent agreement for all layers
373 throughout the troposphere. This suggests that, despite the high bias discussed above, including the
374 $H_2O_{(v)}$ layers could provide important, vertically-resolved information to the machine learning model.
375
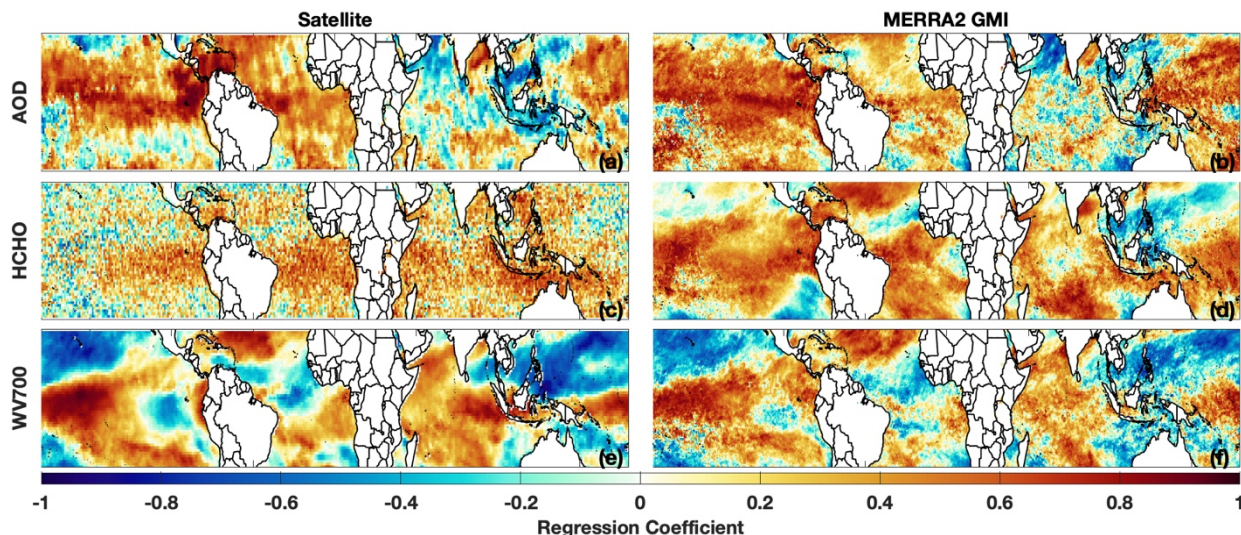
376
377 ***Figure 2:*** Distribution of the regression coefficient of a linear least squares fit of the indicated variable against the
378 MEI for the respective satellite retrieval (a, c, and e) and MERRA2 GMI (b,d, and f) for February. Regressions of
379 AOD are for 2010 to 2019, the years for which we have a one-degree, gridded satellite product, while HCHO and

380   water vapor 700 hPa are for 2005 to 2019. Satellite data are on a 1°×1° grid while model output is at the native
381   model resolution.

382   Modeled accuracy of the HCHO-ENSO relationship is more difficult to assess. While both the OMI
383   retrieval and MERRA2 GMI demonstrate broad regions of anti-correlation between HCHO and ENSO, the
384   correlations with OMI HCHO are weaker and noisier than for the other satellite retrievals. Over much of
385   the domain, HCHO abundance is low, often at or below the retrieval detection limit, suggesting that the
386   HCHO retrieval might not be of sufficient quality to capture ENSO-related variability. We investigate the
387   impacts of the HCHO observational uncertainty in Section 5.

389   Finally, because we use total column O_3 as an input to the GBRT model, we do not evaluate the
390   relationship between ENSO and O_3, as the stratosphere dominates the O_3 column and the ENSO-related
391   variability is mostly confined to the troposphere. Oman et al. (2013) found that a GEOS CCM simulation
392   and a combination of O_3 retrievals from the Microwave Limb Sounder (MLS) and the Tropospheric
393   Emission Spectrometer (TES) exhibited similar ENSO-related variability in the middle and upper
394   troposphere, demonstrating that simulations in the GEOS framework can capture this relationship. If a
395   TES-like satellite retrieval were currently available, it could be a valuable contributor to the GBRT model
396   described here, as it would provide vertically-resolved information about one of the primary drivers of
397   OH production.

399   **4   Tropical tropospheric column OH constrained with observations of its drivers**
400   We now demonstrate the ability of the GBRT model to determine TCOH. First, we show that the GBRT
401   model can reproduce MERRA2 GMI modeled TCOH from a year independent of the training dataset, a
402   so-called "hold out set" (Sect. 4.1). We then input satellite data from one month from each season into
403   the GBRT model to evaluate the realism of the calculated TCOH fields (Sect 4.2).

405   **4.1 Evaluation with an independent year from MERRA2 GMI**
406   The machine learning model is able to capture both the magnitude and the variability of TCOH across
407   each season when applied to MERRA2 GMI output from 2017, a year independent of the training
408   dataset. For August 2017 (Fig. 3b), the predicted TCOH is highly correlated with MERRA2 GMI (r^2 of
409   0.98). TCOH from the machine learning model agrees with the CTM simulation within 4.8% on average.
410   The overall normalized mean bias (NMB) is negligible (-0.1%), although there are some regions of
411   coherent bias (Fig. 3a). Results are similar for February, May, and October 2017 (Fig. S5). The
412   normalized root mean square error for each of these months is comparable to that found for a GBRT
413   parameterization of OH created with a similar methodology that included 27 inputs (Anderson et al.,
414   2022). This suggests that limiting inputs to model variables observable from space does not degrade the
415   ability of the machine learning model to predict TCOH. The low bias and high correlation between the
416   GBRT and MERRA2 GMI TCOH for all four months examined here also suggests that any potential
417   overfitting by the GBRT model is minimal.
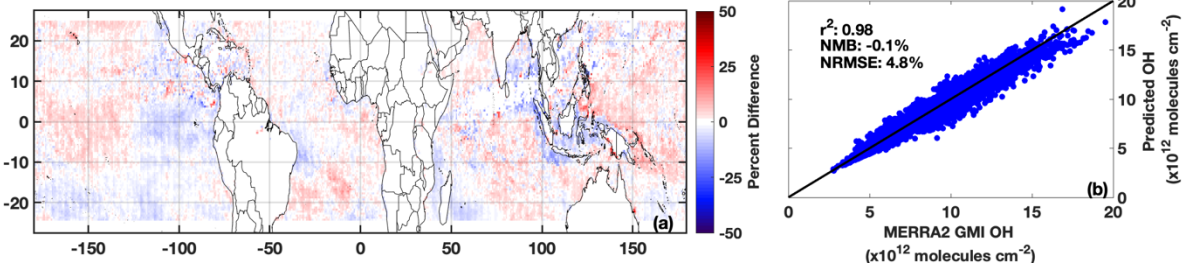
418
419   ***Figure 3:*** Percent difference between TCOH predicted by the machine learning model and that from MERRA2 GMI
420   for August 2017, a month and year omitted from the training dataset **(a)**. A regression of the machine learning TCOH

10

421 against MERRA2 GMI for the same month **(b)**. The r^2 of a linear, least squares regression, along with the normalized
422 mean bias (NMB) and normalized root mean square error (NRMSE), are also indicated.

4.2 TCOH from satellite observations of its drivers
424 We now apply satellite data from the four months corresponding to the ATom campaign (Aug. 2016,
425 Feb. 2017, Oct. 2017, and May 2018) to the GBRT model to determine TCOH fields across the tropics.
426 More details about ATom as well as evaluation of the GBRT model with ATom observations are in
427 Section 5. We use the satellite observations listed in Table 1, all of which have been averaged to the
428 monthly scale and to a $1° \times 1°$ horizontal resolution. We include only grid boxes with observations for
429 all GBRT model inputs and where those observations are within the range of the corresponding inputs
430 from the training dataset. Because the satellite inputs for most species exclude grid boxes with a cloud
431 fraction greater than approximately 30%, the product presented here represents predominantly clear
432 sky conditions.

434 The GBRT model and multi-satellite inputs yield TCOH fields that are geophysically credible based on our
435 current understanding of OH photochemistry. Although the domain-wide average changes little with
436 season, with a minimum of 5.84×10^{12} molecules/cm^2 in May 2018 and a maximum of 6.35×10^{12}
437 molecules/cm^2 in August 2016, the spatial distribution varies widely among the four months (Fig. 4). In
438 both Feb. 2017 and Aug. 2016, TCOH minimizes in the winter hemisphere, consistent with lower OH
439 production due to low insolation. The reverse is true for the summer hemisphere. In addition, TCOH
440 maximizes in regions with strong continental outflow and along coastlines, regions likely to be impacted
441 by anthropogenic and biomass burning emissions of OH drivers.
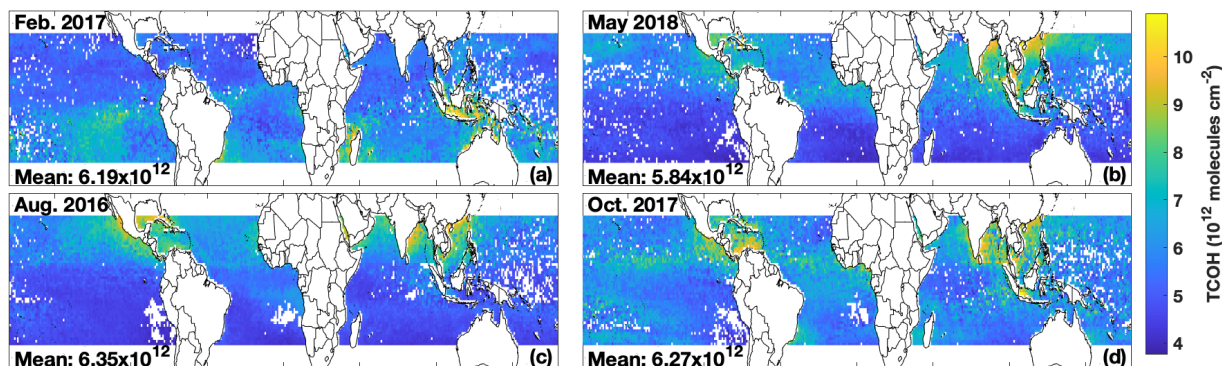
Figure 4: TCOH calculated with the machine learning model using satellite inputs for the months of each ATom
deployment: Feb. 2017 (a), May 2018 (b), Aug. 2016 (c), and Oct. 2017 (d). The mean, domain-wide TCOH value in
molecules/cm^2 for each month is also indicated.

447 In general, TCOH from the multi-satellite product differs in both magnitude and distribution from the
448 MERRA2 GMI simulation. For example, for Feb. 2017, mean MERRA2 GMI TCOH is 6.96×10^{12}
449 molecules/cm^2, 12% higher than the satellite product (Fig. S6). This is consistent with the comparison to
450 *in situ* observations discussed in Section 3.1 where MERRA2 GMI overestimates ATom observations by
451 ~20% and underestimates CH$_4$ lifetime, suggesting that the satellite product is again of reasonable
452 magnitude. While understanding the satellite/model differences in TCOH is beyond the scope of this
453 work, we consider the variety in TCOH spatial distributions generated by the GBRT model to be
454 promising. The difference between the satellite-constrained product and MERRA2 GMI lends some
455 confidence that the GBRT model is not overfit or "tied" to geographic determiners in the training
456 dataset, but rather, is sensitive to variations in the chemical and dynamical drivers of OH. These results
457 all suggest that the methodology presented here can produce a reasonable satellite TCOH product in the

11

458　tropics, with values and distributions independent of the chemistry model used to create the GBRT
459　model.
460
461　**5　Understanding and mitigating potential challenges in using this methodology to constrain TCOH**
462　In this section, we outline possible limitations of the machine learning methodology and the current
463　observational network of the GBRT model inputs and provide potential means to mitigate these
464　limitations where necessary. In section 5.1, we discuss the current lack of sufficient in situ observations
465　to thoroughly evaluate the methodology, highlighting this point by validating the GBRT model with data
466　from the ATom campaign. In section 5.2, we investigate the impacts of random retrieval errors in
467　satellite retrievals on the TCOH product, while in section 5.3, we evaluate the impacts on TCOH when
468　using different satellite retrievals as inputs.
469
470　**5.1 Insufficient in situ observations for thorough independent evaluation**
471　While we demonstrated in Section 4.1 that TCOH calculated with the GBRT model agrees closely with a
472　hold-out set from MERRA2 GMI, it is also important to demonstrate that the GBRT model can replicate
473　observed TCOH from the actual atmosphere. Because the satellite TCOH product shown in Figure 4 is
474　monthly and at a $1^\circ \times 1^\circ$ resolution, however, there are no observations with which to evaluate the
475　product. We can test the ability of the GBRT model to reproduce observed TCOH from field campaigns,
476　however, assuming there are concomitant observations of the input species listed in Table 1. The
477　additional need for tropospheric column values of many of these species severely limits the datasets
478　available for validation. To our knowledge, the ATom campaign is the only source of the required inputs
479　with enough observations to attempt a limited validation.
480
481　During ATom (Thompson et al., 2022), scientists measured a suite of air quality and climate relevant
482　trace gases and aerosols throughout the atmosphere above the remote Pacific and Atlantic. ATom took
483　place in four parts: ATom 1 (July – August 2016), ATom 2 (January – February 2017), ATom 3 (September
484　– October 2017), and ATom 4 (April – May 2018). During each deployment, flights consisted of a series
485　of ascents and descents across all tropical latitudes over the Pacific and Atlantic Oceans. This allows for
486　the calculation of tropospheric column content of the observed species and evaluation of the machine
487　learning model across most latitudes of our study domain and across all seasons.
488
489　To evaluate the GBRT model performance, we calculated TCOH using a modified GBRT model and
490　observations from the ATom deployments as inputs. We then compared the values to the observed OH
491　columns. To calculate the column values from the observations, we averaged data into 25 hPa pressure
492　bins for each ATom profile. We filled in missing data using a log-linear interpolation and then integrated
493　the column. Our analysis here includes only profiles with observations of all necessary species, that
494　spanned at least 700 hPa, and where less than 25% of the pressure bin values were interpolated. We
495　also omitted any profiles that had pressure bins with negative OH values. In addition, we restrict our
496　analysis to latitudes within 25° of the equator and profiles conducted between 12:00 and 15:00 LST.
497　Values for total column O_3, AOD, and SSTs, for which there were no observations during ATom, were
498　taken from the MERRA2 GMI simulation from the grid box closest to the center of the respective profile.
499　Because ATom profiles did not span the entire tropospheric column, we trained a separate GBRT model
500　where OH and all tropospheric column input variables were substituted with columns spanning 990 –
501　250 hPa, the median range of ATom profiles. This allows for a more direct comparison between
502　observed and modeled TCOH. The spatial distribution of the valid ATom columns and the corresponding
503　columns calculated with the GBRT model are shown in Figure S7.
504
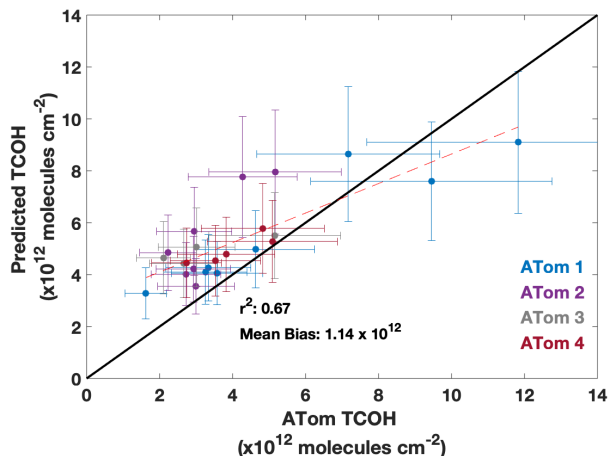
Figure 5: Regression of TCOH observed from the ATom deployments against that predicted from the GBRT model. Error bars represent the 2σ observational uncertainty as reported in Brune et al. (2020) and the GBRT uncertainty described in Section 5.2. The r^2 of a linear least squares fit and the mean bias are also shown.

The GBRT model captures the variability of the observed TCOH, and, while there is a modest overall high bias, the median normalized absolute error of 28.3% is within observational uncertainty. When applied to all ATom deployments, predicted TCOH is correlated with the observations with an r^2 of 0.67 and a mean bias of 1.14×10^{12} molecules/cm^2 (Fig.5). Many of the data points agree within the combined modeled and observational uncertainty. The r^2 values for individual deployments are 0.88 for ATom 1, 0.73 for ATom2, and 0.78 for ATom 3 and 4. The level of agreement between observed and predicted OH is comparable or better than that of other methods to infer OH from space. For example, Pimlott et al. (2022) found an r of 0.78 (r^2 = 0.61) when estimating ATom OH using a steady state approach, with r values ranging from 0.51 to 0.85 (r^2 of 0.26 to 0.72) for the different deployments. The level of agreement we show here therefore demonstrates the validity of the machine learning method to capture the variability of OH.

The source of the model/measurement disagreement, with over- and underprediction at low and high column content respectively, is unclear, although there are multiple potential error sources. For example, a typical profile taken during ATom spanned 300 – 400 km in latitude, disconnecting the top and bottom of the profile in space. This is in contrast to the data used to train the model, which were vertical columns over one location. This could lead to a degradation in model performance when applied to ATom, since the columns are not directly analogous to the training dataset. These effects are likely limited because ATom observations are in the remote atmosphere, where the spatial distribution of relevant species is likely to be more homogeneous than over land.

Further, there is a known interference with the ATom NO_2 observations, suggesting another possible contributor to disagreement between measured and modeled OH. Because of thermal degradation of NO_2 reservoir species, such as organic nitrates and peroxyacetyl nitrate, in the instrument inlet, ATom NO_2 observations are likely biased high (Silvern et al., 2018;Shah et al., 2023;Nault et al., 2015). To test the potential impact of NO_2 on the predicted OH columns, we applied the ATom observations to a model that omits NO_2 as an input. Removing NO_2 increases the r^2 to 0.74, decreases the mean bias to 0.82×10^{12} molecules/cm^2, and decreases the median normalized absolute error slightly to 25.7% (Fig. S8). These improvements in performance suggest that errors in NO_2 could be contributing to the measurement/model differences. Omitting NO_2 does, however, likely introduce additional errors as NO_x compounds are essential to OH production in some regions of the atmosphere. When we apply the hold

540   out set from MERRA2 GMI to this model, for example, the NRMSE increases by approximately 50%,
541   highlighting the importance of keeping NO_2 as an input variable.

542

543   For more certain evaluation of the GBRT model with observations, greater certainty in the in situ NO_2
544   observations is needed. Although the in situ observations are insufficient to evaluate the absolute
545   accuracy of the product, the results presented here demonstrate that a machine learning model trained
546   on data from a CTM simulation can capture TCOH variability in the actual atmosphere and suggest that
547   predicted OH columns agree with observations within instrumental uncertainty.

548

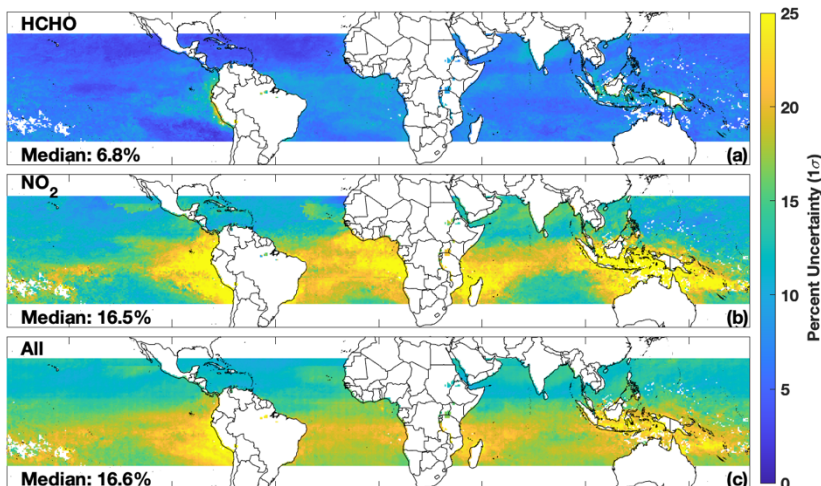549   **5.2 Impacts of uncertainties in the satellite retrievals on TCOH**
550   In the remote atmosphere where HCHO and NO_2 abundances are low, retrieval uncertainty of an
551   individual pixel for both species can be on the order of 100% and is often reflective of the *a priori*
552   (González Abad et al., 2015;Lamsal et al., 2021). Given the importance of these species to the GBRT
553   model as well as to OH chemistry, it is necessary to determine how the propagation of the retrieval
554   uncertainties from these and other model inputs impacts the predicted TCOH.

555

556   We determined the total uncertainty in TCOH from all inputs as well as the resultant uncertainty from
557   each individual input for Feb. 2017. First, we estimated an average retrieval uncertainty for each input
558   based on reported values in the retrieval files or from the literature (Table S1). We note that for NO_2
559   and HCHO we use a fit uncertainty for a single retrieval. Because we are using monthly-averaged data at
560    $1° \times 1°$ horizontal resolution, this likely significantly overestimates the actual uncertainty in these
561   retrievals as the random error from individual pixels will tend to cancel when averaged over such large
562   spatial and temporal scales. Our results are therefore an upper bound on the estimated TCOH
563   uncertainty.

564

565   Next, for each grid box and model input, we created a Gaussian distribution of 2000 values with the
566   modeled value for Feb. 2017 as the mean and the estimated uncertainty as the standard deviation. For
567   each input, we then ran the GBRT model 2000 times to create a distribution of predicted TCOH values
568   for each grid box. The normalized uncertainty in TCOH attributable to a given input is the ratio of the
569   standard deviation of the resultant distribution divided by the mean value. We repeated this process
570   individually for all inputs. In addition, to estimate a total uncertainty in TCOH, we varied all inputs
571   simultaneously with the same Gaussian distributions described above.

572

573   Uncertainty from the NO_2 retrieval, and to a lesser extent HCHO, dominates the total uncertainty in the
574   TCOH product but is of a magnitude comparable to that of in situ OH observations. Median TCOH 1σ
575   uncertainty resulting from NO_2 is 16.5%, with maxima in the remote atmosphere in regions where NO_2
576   columns are low. Median uncertainty in TCOH resulting from HCHO is 7%, averaged over the study
577   domain, despite the large uncertainty in the HCHO retrieval itself. In contrast to NO_2, uncertainties in
578   TCOH resulting from HCHO maximize in regions with higher HCHO columns (Fig. 6). The magnitude of
579   that uncertainty is likely an overestimate as the actual retrieval uncertainty for HCHO in these regions is
580   significantly lower than the value assumed for the error analysis. In comparison, median TCOH
581   uncertainties resulting from other inputs are 2.9% or less (Figs. S9 and S10). Total TCOH uncertainty is
582   16.6% and is dominated by the NO_2 uncertainty. This uncertainty analysis is in general agreement with
583   the model feature importance (Supplementary Fig. 11), a measure of the relative importance of GBRT
584   model inputs, where HCHO and NO_2 consistently have the largest values of the satellite inputs.

585

Figure 6: Normalized 1σ uncertainty in the satellite TCOH product due to uncertainties in the HCHO (a) and NO2 (b) retrievals. The combined uncertainty from all input species is shown in panel c.

These results demonstrate that the satellite retrieval inputs to the machine learning model are of sufficient quality to produce a meaningful TCOH data product when averaged over large spatial and temporal scales. The 2σ uncertainty in TCOH resulting from the uncertainties in these retrievals is on the order of that reported for in situ OH observations (Brune et al., 2020). As discussed earlier, this is also likely an upper bound on the uncertainty from random retrieval errors, and uncertainties could be reduced through further averaging, although at the expense of reduced spatial and temporal resolution. Improving the satellite retrievals of NO_2 and HCHO in the remote atmosphere, using retrievals with less noise over the remote atmosphere such as HCHO from OMPS (González Abad et al., 2016), or incorporating data from satellites with higher resolution, such as TROPOMI, could also reduce the uncertainty in their retrievals and thus in TCOH. As discussed in the next section, however, systematic biases between satellite retrievals can also lead to uncertainties in the TCOH.

5.3   Sensitivity of TCOH to different satellite retrievals of GBRT inputs

The satellite retrievals listed in Table 1 provide the benefit of a long record, with data from most retrievals available from at least 2005 to the present. Such a rich dataset would allow for long-term trend analysis of TCOH. These instruments are near the end of their life cycle, however, so it is instructive to see how retrievals from newer satellites impact the predicted TCOH from the GBRT model. In addition, although these newer satellites, such as TROPOMI, have a significantly shorter observational record than those in Table 1, TROPOMI also has finer spatial resolution and the added advantage of providing retrievals for CO, NO_2, O_3, HCHO, and $H_2O_{(v)}$. Using retrievals of multiple species from the same instrument could negate errors resulting from differences in viewing geometry as well as from overpass time. Here, we investigate the effects of applying retrievals from TROPOMI to the machine learning model and compare them to the results from the product described in Section 4, highlighting potential impacts resulting from instrumental differences as well as those resulting from differences in retrieval algorithms. The results emphasize the need for thorough retrieval validation in the remote atmosphere, particularly of NO_2.

5.3.1   Description of TROPOMI and a modified GBRT model

TROPOMI, a successor instrument to OMI, is a spectrometer covering portions of the ultraviolet, visible, and infrared spectrum (Veefkind et al., 2012). It is located onboard the Sentinel 5 Precursor satellite, which is polar orbiting and has a local overpass time of approximately 13:30. Horizontal resolution for

15

620   the month examined here (May 2018) is as high as 7 km × 3.5 km at nadir. We have gridded the Level 2
621   product for each species to a 1° × 1° resolution and averaged the data to the monthly scale, applying the
622   recommended quality flags and filtering for cloud fraction greater than 30%.

624   We use two different retrievals of TROPOMI NO_2 for this analysis. First, we use the KNMI (Royal
625   Netherlands Meteorological Institute) NO_2 retrieval (van Geffen et al., 2020), which is based on the
626   DOMINO (Dutch OMI NO_2 product) retrieval developed for the OMI instrument. Wang et al. (2020)
627   found that this retrieval was biased high when compared to ship-based observations from a MAX-DOAS
628   instrument over the remote oceans, while Verhoelst et al. (2021) found good agreement between the
629   retrieval and ground-based observations in Reunion. In addition, we use the MINDS (Multi-Decadal
630   Nitrogen Dioxide and Derived Products from Satellites) retrieval, which uses the same algorithm as for
631   the OMI product described in Section 2 (Lamsal et al., 2022). This retrieval has not been evaluated in
632   the remote tropics.

634   We also use TROPOMI retrievals of HCHO, $H_2O_{(v)}$ column, total column O_3, and CO. The HCHO retrieval
635   (De Smedt et al., 2018) was found to have a 30% low bias with respect to an OMI retrieval using the
636   same algorithm due to differences in cloud processing (De Smedt et al., 2021). While evaluation in the
637   remote tropics is limited, the TROPOMI retrieval does overestimate HCHO in polluted regions (De Smedt
638   et al., 2021) when compared to ground-based observations. The TROPOMI $H_2O_{(v)}$ (Chan et al., 2022)
639   retrieval has a slight dry bias with comparison to other satellite products, while the total column O_3
640   retrieval (Garane et al., 2019) agrees within 0 – 1.5% with ground-based observations. Finally, the CO
641   retrieval (Borsdorff et al., 2019) agrees with MOPITT over the oceans within 3% on average (Martínez-
642   Alonso et al., 2020). TROPOMI does not have an equivalent retrieval of the AIRS $H_2O_{(v)}$ layers.

644   To calculate TCOH using TROPOMI data, we trained a separate machine learning model using all inputs
645   from Table 1 except the water vapor layers, for which there are no TROPOMI retrievals. Removal of the
646   layers from the machine learning model does not significantly degrade performance. For example, for
647   May 2017, removing the $H_2O_{(v)}$ layers from the model, increases the NRMSE from 5.34% to 5.73% when
648   applying the GBRT model to the hold out set. For this new model, we then calculate TCOH using
649   TROPOMI data, including the KNMI NO_2 retrieval. For SSTs and AOD, we use the MUR and MODIS
650   products respectively. While TROPOMI does have an aerosol product, the UV aerosol index, the
651   corresponding output from the MERRA2 GMI simulation is unavailable. We refer to this TCOH as the
652   TROPOMI-KNMI product. We have also calculated TCOH using the satellite retrievals in Table 1, except
653   for the water vapor layers, using this GBRT model, and refer to that as the OMI/MOPITT/AIRS product.
654   We restrict our analysis to May 2018, the only month for which we have TROPOMI water vapor data.

656   **5.3.2   TROPOMI data applied to the GBRT model**
657   TCOH from the TROPOMI-KNMI product is higher than that from the OMI/MOPITT/AIRS product for May
658   2018. Figure 7 shows TCOH calculated from the TROPOMI-KNMI product as well as the percent
659   difference between the two products. While there is modest correlation between the two (r^2 = 0.63),
660   the TROPOMI product is 27.6% higher than the OMI/MOPITT/AIRS product, with higher values across
661   almost the entire domain. Differences between the products are most pronounced in the Indian Ocean
662   and off the coasts of Indonesia and the Philippines.

664   In general, observations from TROPOMI agree with those from the satellites in Table 1, with the
665   exception of NO_2 and HCHO. Ozone, $H_2O_{(v)}$, and CO from TROPOMI are highly correlated (r^2 of 0.85 or
666   higher) and agree within 10% on average (Fig. S12) with their respective retrievals from OMI, MOPITT,
667   and AIRS. On the other hand, TROPOMI KNMI-NO_2 is systematically higher (145% on average), and

668   TROPOMI HCHO is 20% lower than their corresponding OMI retrievals. The higher TCOH from the
669   TROPOMI product is consistent with the increase in NO_2, which would lead to higher secondary
670   production of OH. Further, while TROPOMI KNMI-NO_2 is modestly correlated with OMI NO_2 (r^2 = 0.61),
671   TROPOMI and OMI HCHO are not correlated (r^2 = 0.23), highlighting the difficulty of the HCHO retrieval.
672   Note that we are not seeking to determine which retrieval, if any, is more accurate. We are highlighting
673   the differences to emphasize the impact that systematic differences in retrieval magnitudes of GBRT
674   model inputs can have on the resultant TCOH.

675
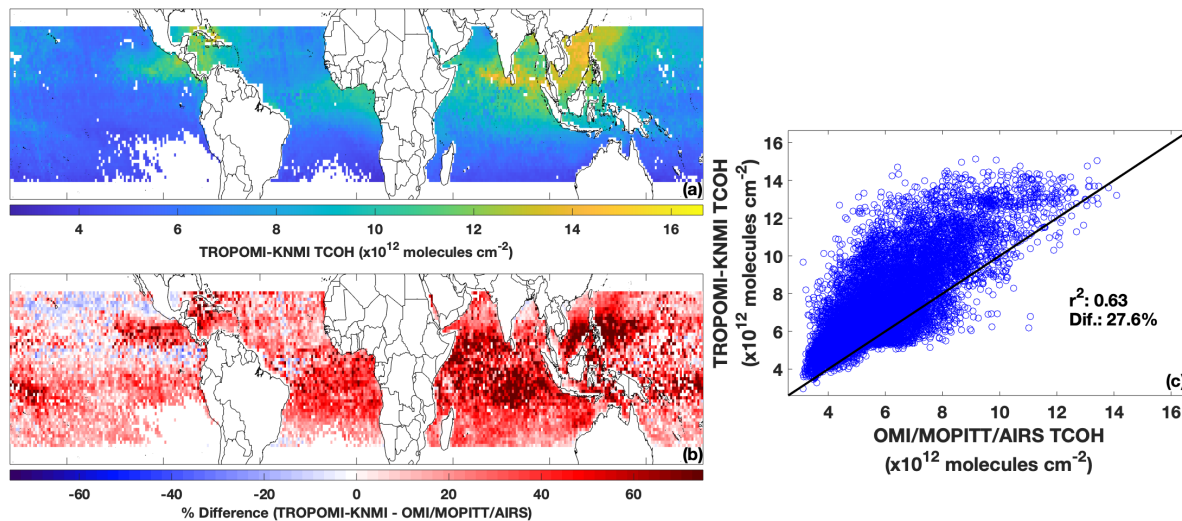
676
677   **Figure 7:** TCOH for May 2018 determined using TROPOMI inputs, including the KNMI NO_2 retrieval (a). The
678   difference between the TROPOMI and multi-satellite product is shown in (b). Panel (c) shows the regression of
679   TCOH calculated from TROPOMI against that calculated from retrievals from MOPITT, OMI, and AIRS as well as the
680   percent difference between the two TCOH products.

681   NO_2 drives the differences between the two TCOH products. To determine the impacts of the different
682   TROPOMI inputs on the TCOH product, we individually swapped each TROPOMI input into the
683   OMI/MOPITT/AIRS product, replacing the corresponding input from Table 1. We then determined the
684   difference in TCOH from the OMI/MOPITT/AIRS product that does not include TROPOMI. While this
685   method will not yield the exact contribution from a particular retrieval because of the non-linear nature
686   of OH chemistry, it does yield information about the relative importance of each species. Swapping in
687   TROPOMI CO, $H_2O_{(v)}$, and O_3 changed TCOH by less than 2%, while using TROPOMI HCHO increased
688   TCOH by 3%. In contrast, TROPOMI NO_2 increased TCOH by 29%, showing that the higher TCOH in the
689   TROPOMI product is driven by differences in NO_2.

690
691   The increased TCOH in the TROPOMI product likely results from a combination of differences in the NO_2
692   retrieval algorithm as well as instrumental differences. Comparison of the KNMI and MINDS retrievals
693   illustrate this point. When compared to OMI, the MINDS NO_2 retrieval is 58% higher for May 2018, as
694   compared to 145% higher for the KNMI retrieval. The closer agreement is unsurprising since the MINDS
695   NO_2 uses the same retrieval algorithm as for OMI. Substituting the MINDS NO_2 as an input to the
696   TROPOMI product (TROPOMI-MINDS product) reduces the difference with respect to the
697   OMI/MOPITT/AIRS product to 18% (Fig. S13). While this is an improvement in agreement, the
698   differences in TCOH as well as the lack of change in r^2 value still suggest that differences between OMI
699   and TROPOMI unrelated to the retrieval algorithm account for some of the discrepancy. In addition, the
700   training dataset does not take TROPOMI averaging kernels and shape factors into account, which could
701   also contribute to the observed differences.

17

702
703 The results here demonstrate the sensitivity of the methodology to any systematic bias in the input
704 retrievals. As with the random error analysis, the level of uncertainty introduced by these biases is low
705 enough to allow for a meaningful OH product. Despite these differences, the methodology to determine
706 TCOH using machine learning that we have presented here still captures the variability in TCOH,
707 consistent with the ATom evaluation outlined in Section 5.1. To reduce the uncertainty of TCOH, better
708 evaluation of NO_2 in the remote atmosphere is needed to determine which retrievals, if any, are
709 accurate.
710
711 **6   Discussion and recommendations for future observations**
712 The method of estimating clear-sky TCOH presented here has the potential to increase our
713 understanding of the atmospheric oxidation capacity. Because of the long record of observations from
714 MOPITT, OMI, AIRS, and MODIS, we can calculate tropical TCOH from 2005 to the present, and since the
715 methodology is not constrained to a particular satellite, newer satellite missions could extend the
716 dataset beyond the end of these instruments' lifetimes. In addition, this methodology will provide sub-
717 hemispheric information on OH variability, supplementing information available from MCF inversions.
718
719 The methodology could be expanded to the extra-tropics and over land, allowing for global constraints
720 on OH. Expansion over land will likely require additional satellite retrievals, like that of isoprene (Wells
721 et al., 2020), in regions with more complex VOC chemistry than in the remote atmosphere. Expanding
722 this product beyond the tropics could increase understanding of global CH_4, CO, and VOC trends and
723 variability and allow for a wider range of satellite retrievals as inputs. For example, current and
724 upcoming geostationary air quality satellites such as Sentinel 4, TEMPO (Tropospheric Emissions:
725 Monitoring of Pollution), and GEMS (Geostationary Environment Monitoring Spectrometer) could
726 provide retrievals of most of the necessary inputs to the machine learning model, allowing for the
727 understanding of diurnal variability in TCOH and potentially in the diurnal variability of ozone production
728 (Zhu et al., 2022a).
729
730 A similar methodology could likely be used to determine OH at different layers of the atmosphere.
731 Because CH_4 loss is not evenly distributed throughout the tropospheric column, vertically resolved OH
732 would better help inform this process. Vertically-resolved OH could also help understand differences in
733 OH drivers in the upper and lower troposphere (Spivakovsky et al., 1990;Lelieveld et al., 2016), which
734 can often be decoupled from the column. While column inputs, such as those discussed here, could be
735 used, the inclusion of vertically resolved satellite retrievals, such as the AIRS $H_2O_{(v)}$ layers, would provide
736 additional information. Tropospheric O_3 at different atmospheric layers, such as that previously
737 provided by the TES satellite, could also be invaluable here, as O_3 is a large driver of primary OH
738 production.
739
740 Satellite-derived OH would also a provide a much-needed, observational constraint on OH variability in
741 global chemistry models. Because the methodology can capture variability in TCOH of both
742 observations and 3-dimensional model output, TCOH trends from a satellite-constrained product could
743 be used to evaluate modeled trends and as well as the spatial variability resulting from events like ENSO.
744 While the satellite-derived OH could not explicitly indicate the cause of differences, the spatial
745 distribution of the differences as well as differences in observed and modeled machine learning model
746 inputs could indicate potential dynamical or emission sources of error in the 3D model.
747
748 Further, the combination of the satellite-derived OH and the machine learning model could help identify
749 the impacts of any diagnosed errors in emissions inventories as well as the impacts of unexpected

18

750 events, such as COVID-19-related shutdowns, on TCOH. For example, if there are significant
751 discrepancies between observed and modeled NO_2 in a specific region of the atmosphere, the satellite
752 NO_2 could be scaled to more closely match the 3D model values and then be input into the machine
753 learning model. The difference in TCOH would then indicate the relative impact of the model error. This
754 would serve as a computationally efficient complement to other methodologies constraining models
755 with observations (e.g. Miyazaki et al., 2020;Miyazaki et al., 2021) to identify the impacts of these errors
756 on the atmospheric oxidation capacity. A similar methodology could be used for unexpected events that
757 significantly impact emissions of OH drivers, allowing for quick determination of their potential impacts
758 on the atmospheric oxidation capacity before emissions inventories could be revised.
759
760 While we have shown that the methodology captures the variability of observed OH and generally
761 agrees with observations within measurement uncertainty, it is unclear whether differences result from
762 GBRT model deficiencies or structural differences between the *in situ* observations and the training
763 dataset. Additional field campaigns with observations of OH and the GBRT model inputs would allow for
764 a more thorough evaluation of both the OH product and the methodology itself. Such a field campaign
765 would need to provide complete tropospheric columns of all species and cover less horizontal distance
766 than the ATom profiles (e.g. from spiral flight patterns). In situ observations of NO_2 without significant
767 interference from NO_X reservoir species are also needed to reduce uncertainty. Alternatively, NO_2 and
768 other species could be measured through aircraft-based remote sensing. Finally, repeated sampling over
769 the same locations for multiple days within a defined area would allow for meaningful statistical analysis
770 while also allowing for the comparison of TCOH columns calculated from satellite observations.
771
772 Finally, accuracy of the TCOH product is dependent on the accuracy of the satellite retrievals input into
773 the machine learning model, with the NO_2 retrieval having the largest effect. To reduce the uncertainty
774 of the TCOH product, more information about the accuracy of individual NO_2 retrievals is required.
775 Currently, there is little validation of OMI and TROPOMI NO_2 retrievals in the remote, tropical
776 atmosphere, so it is difficult to assess which retrievals, if any, are correct. Recent efforts, such as the
777 QA4ECV (Quality Assurance for the Essential Climate Variables), to improve NO_2 retrieval algorithms
778 have reduced uncertainty, particularly over land (Boersma et al., 2018), although it is unclear how the
779 accuracy of these retrievals translates to the remote tropics as validation data are still extremely limited.
780 Even retrievals of TROPOMI and OMI made with the same algorithm show differences, suggesting that
781 instrumental differences could also affect the results. Future satellite missions should focus on trying to
782 reduce the uncertainty in NO_2 retrievals, particularly in the remote atmosphere, both through
783 improvements in instrument design and algorithm development.
784
785 **7 Data Availability**
786 Output from the MERRA2 GMI simulation are publicly available at https://acd-
787 ext.gsfc.nasa.gov/Projects/GEOSCCM/MERRA2GMI/ (NASA Goddard Space Flight Center, 2023). All
788 satellite products, except for TROPOMI water vapor, are available at https://disc.gsfc.nasa.gov (GES
789 DISC, 2023). Data from the ATom campaign are located at https://daac.ornl.gov (Wofsy et al., 2021).
790
791 **8 Author contributions**
792 DCA wrote the manuscript, performed the data analysis, and created the GBRT model. DCA, BND, JMN,
793 and MBFC developed the idea for the methodology. SAS performed three-dimensional modeling for the
794 work. JMN provided advice on machine learning. JL helped perform data analysis. All authors helped
795 develop ideas for the analysis and contributed to the manuscript.
796
797 **9 Competing Interests**

809

810 **10. References**

811

812 Anderson, D. C., Nicely, J. M., Salawitch, R. J., Canty, T. P., Dickerson, R. R., Hanisco, T. F., Wolfe, G. M.,
813 Apel, E. C., Atlas, E., Bannan, T., Bauguitte, S., Blake, N. J., Bresch, J. F., Campos, T. L., Carpenter, L. J.,
814 Cohen, M. D., Evans, M., Fernandez, R. P., Kahn, B. H., Kinnison, D. E., Hall, S. R., Harris, N. R., Hornbrook,
815 R. S., Lamarque, J. F., Le Breton, M., Lee, J. D., Percival, C., Pfister, L., Pierce, R. B., Riemer, D. D., Saiz-
816 Lopez, A., Stunder, B. J., Thompson, A. M., Ullmann, K., Vaughan, A., and Weinheimer, A. J.: A pervasive
817 role for biomass burning in tropical high ozone/low water structures, Nat Commun, 7, 10267,
818 10.1038/ncomms10267, 2016.

819 Anderson, D. C., Duncan, B. N., Fiore, A. M., Baublitz, C. B., Follette-Cook, M. B., Nicely, J. M., and Wolfe,
820 G. M.: Spatial and temporal variability in the hydroxyl (OH) radical: understanding the role of large-scale
821 climate features and their influence on OH through its dynamical and photochemical drivers,
822 Atmospheric Chemistry and Physics, 21, 6481-6508, 10.5194/acp-21-6481-2021, 2021.

823 Anderson, D. C., Follette-Cook, M. B., Strode, S. A., Nicely, J. M., Liu, J., Ivatt, P. D., and Duncan, B. N.: A
824 machine learning methodology for the generation of a parameterization of the hydroxyl radical, Geosci.
825 Model Dev., 15, 6341-6358, 10.5194/gmd-15-6341-2022, 2022.

826 Bedka, S., Knuteson, R., Revercomb, H., Tobin, D., and Turner, D.: An assessment of the absolute
827 accuracy of the Atmospheric Infrared Sounder v5 precipitable water vapor product at tropical,
828 midlatitude, and arctic ground-truth sites: September 2002 through August 2008, Journal of Geophysical
829 Research: Atmospheres, 115, D17310, https://doi.org/10.1029/2009JD013139, 2010.

830 Boersma, K. F., Eskes, H. J., Richter, A., De Smedt, I., Lorente, A., Beirle, S., van Geffen, J. H. G. M., Zara,
831 M., Peters, E., Van Roozendael, M., Wagner, T., Maasakkers, J. D., van der A, R. J., Nightingale, J., De
832 Rudder, A., Irie, H., Pinardi, G., Lambert, J. C., and Compernolle, S. C.: Improving algorithms and
833 uncertainty estimates for satellite NO2 retrievals: results from the quality assurance for the essential
834 climate variables (QA4ECV) project, Atmos. Meas. Tech., 11, 6651-6678, 10.5194/amt-11-6651-2018,
835 2018.

836 Borsdorff, T., aan de Brugh, J., Schneider, A., Lorente, A., Birk, M., Wagner, G., Kivi, R., Hase, F., Feist, D.
837 G., Sussmann, R., Rettinger, M., Wunch, D., Warneke, T., and Landgraf, J.: Improving the TROPOMI CO
838 data product: update of the spectroscopic database and destriping of single orbits, Atmos. Meas. Tech.,
839 12, 5443-5455, 10.5194/amt-12-5443-2019, 2019.

840 Brune, W. H., Miller, D. O., Thames, A. B., Allen, H. M., Apel, E. C., Blake, D. R., Bui, T. P., Commane, R.,
841 Crounse, J. D., Daube, B. C., Diskin, G. S., DiGangi, J. P., Elkins, J. W., Hall, S. R., Hanisco, T. F., Hannun, R.
842 A., Hintsa, E. J., Hornbrook, R. S., Kim, M. J., McKain, K., Moore, F. L., Neuman, J. A., Nicely, J. M., Peischl,
843 J., Ryerson, T. B., St. Clair, J. M., Sweeney, C., Teng, A. P., Thompson, C., Ullmann, K., Veres, P. R.,
844 Wennberg, P. O., and Wolfe, G. M.: Exploring Oxidation in the Remote Free Troposphere: Insights From
845 Atmospheric Tomography (ATom), Journal of Geophysical Research: Atmospheres, 125, e1019JD031685,
846 10.1029/2019jd031685, 2020.

847 Buchholz, R. R., Deeter, M. N., Worden, H. M., Gille, J., Edwards, D. P., Hannigan, J. W., Jones, N. B.,
848 Paton-Walsh, C., Griffith, D. W. T., Smale, D., Robinson, J., Strong, K., Conway, S., Sussmann, R., Hase, F.,
849 Blumenstock, T., Mahieu, E., and Langerock, B.: Validation of MOPITT carbon monoxide using ground-
850 based Fourier transform infrared spectrometer data from NDACC, Atmos. Meas. Tech., 10, 1927-1956,
851 10.5194/amt-10-1927-2017, 2017.

852 Burnett, C. R., and Minschwaner, K.: Continuing development in the regime of decreased atmospheric
853 column OH at Fritz Peak, Colorado, Geophysical Research Letters, 25, 1313-1316,
854 https://doi.org/10.1029/98GL01062, 1998.

855 Chan, K. L., Xu, J., Slijkhuis, S., Valks, P., and Loyola, D.: TROPOspheric Monitoring Instrument
856 observations of total column water vapour: Algorithm and validation, Science of The Total Environment,
857 821, 153232, https://doi.org/10.1016/j.scitotenv.2022.153232, 2022.

858 Chen, T., and Guestrin, C.: XGBoost: A Scalable Tree Boosting System, KDD '16: Proceedings of the 22nd
859 ACM SIGKDD International Conference on Knowledge Discovery and Data Mining, 13 - 17 Aug. 2016,
860 785-794, San Francsisco, CA, USA, https://doi.org/10.1145/2939672.2939785, 2016.

861 Chin, T. M., Vazquez-Cuervo, J., and Armstrong, E. M.: A multi-scale high-resolution analysis of global sea
862 surface temperature, Remote Sensing of Environment, 200, 154-169,
863 https://doi.org/10.1016/j.rse.2017.07.029, 2017.

864 Choi, S., Lamsal, L. N., Follette-Cook, M., Joiner, J., Krotkov, N. A., Swartz, W. H., Pickering, K. E.,
865 Loughner, C. P., Appel, W., Pfister, G., Saide, P. E., Cohen, R. C., Weinheimer, A. J., and Herman, J. R.:
866 Assessment of NO2 observations during DISCOVER-AQ and KORUS-AQ field campaigns, Atmos. Meas.
867 Tech., 13, 2523-2546, 10.5194/amt-13-2523-2020, 2020.

868 De Smedt, I., Theys, N., Yu, H., Danckaert, T., Lerot, C., Compernolle, S., Van Roozendael, M., Richter, A.,
869 Hilboll, A., Peters, E., Pedergnana, M., Loyola, D., Beirle, S., Wagner, T., Eskes, H., van Geffen, J.,
870 Boersma, K. F., and Veefkind, P.: Algorithm theoretical baseline for formaldehyde retrievals from S5P
871 TROPOMI and from the QA4ECV project, Atmospheric Measurement Techniques, 11, 2395-2426,
872 10.5194/amt-11-2395-2018, 2018.

873 De Smedt, I., Pinardi, G., Vigouroux, C., Compernolle, S., Bais, A., Benavent, N., Boersma, F., Chan, K. L.,
874 Donner, S., Eichmann, K. U., Hedelt, P., Hendrick, F., Irie, H., Kumar, V., Lambert, J. C., Langerock, B.,
875 Lerot, C., Liu, C., Loyola, D., Piters, A., Richter, A., Rivera Cárdenas, C., Romahn, F., Ryan, R. G., Sinha, V.,
876 Theys, N., Vlietinck, J., Wagner, T., Wang, T., Yu, H., and Van Roozendael, M.: Comparative assessment
877 of TROPOMI and OMI formaldehyde observations and validation against MAX-DOAS network column
878 measurements, Atmos. Chem. Phys., 21, 12561-12593, 10.5194/acp-21-12561-2021, 2021.

879 Deeter, M. N., Edwards, D. P., Francis, G. L., Gille, J. C., Mao, D., Martínez-Alonso, S., Worden, H. M.,
880 Ziskin, D., and Andreae, M. O.: Radiance-based retrieval bias mitigation for the MOPITT instrument: the
881 version 8 product, Atmospheric Measurement Techniques, 12, 4561-4580, 10.5194/amt-12-4561-2019,
882 2019.

883 Duncan, B., Portman, D., Bey, I., and Spivakovsky, C.: Parameterization of OH for efficient computation in
884 chemical tracer models, Journal of Geophysical Research: Atmospheres, 105, 12259-12262,
885 10.1029/1999JD901141, 2000.

886 Duncan, B. N., Strahan, S. E., Yoshida, Y., Steenrod, S. D., and Livesey, N.: Model study of the cross-
887 tropopause transport of biomass burning pollution, Atmos. Chem. Phys., 7, 3713-3736, 10.5194/acp-7-
888 3713-2007, 2007.

889 Elith, J., Leathwick, J. R., and Hastie, T.: A working guide to boosted regression trees, J Anim Ecol, 77,
890 802-813, 10.1111/j.1365-2656.2008.01390.x, 2008.

891 Garane, K., Koukouli, M. E., Verhoelst, T., Lerot, C., Heue, K. P., Fioletov, V., Balis, D., Bais, A., Bazureau,
892 A., Dehn, A., Goutail, F., Granville, J., Griffin, D., Hubert, D., Keppens, A., Lambert, J. C., Loyola, D.,
893 McLinden, C., Pazmino, A., Pommereau, J. P., Redondas, A., Romahn, F., Valks, P., Van Roozendael, M.,
894 Xu, J., Zehner, C., Zerefos, C., and Zimmer, W.: TROPOMI/S5P total ozone column data: global ground-
895 based validation and consistency with other satellite missions, Atmos. Meas. Tech., 12, 5263-5287,
896 10.5194/amt-12-5263-2019, 2019.

897 Gelaro, R., McCarty, W., Suarez, M. J., Todling, R., Molod, A., Takacs, L., Randles, C., Darmenov, A.,
898 Bosilovich, M. G., Reichle, R., Wargan, K., Coy, L., Cullather, R., Draper, C., Akella, S., Buchard, V., Conaty,
899 A., da Silva, A., Gu, W., Kim, G. K., Koster, R., Lucchesi, R., Merkova, D., Nielsen, J. E., Partyka, G.,
900 Pawson, S., Putman, W., Rienecker, M., Schubert, S. D., Sienkiewicz, M., and Zhao, B.: The Modern-Era
901 Retrospective Analysis for Research and Applications, Version 2 (MERRA-2), J Clim, Volume 30, 5419-
902 5454, 10.1175/JCLI-D-16-0758.1, 2017.

903 GES DISC: Earth Science Data at NASA, available at https://disc.gsfc.nasa.gov, last access: 6 Mar. 2023.

904 González Abad, G., Liu, X., Chance, K., Wang, H., Kurosu, T. P., and Suleiman, R.: Updated Smithsonian
905 Astrophysical Observatory Ozone Monitoring Instrument (SAO OMI) formaldehyde retrieval,
906 Atmospheric Measurement Techniques, 8, 19-32, 10.5194/amt-8-19-2015, 2015.

907 González Abad, G., Vasilkov, A., Seftor, C., Liu, X., and Chance, K.: Smithsonian Astrophysical Observatory
908 Ozone Mapping and Profiler Suite (SAO OMPS) formaldehyde retrieval, Atmospheric Measurement
909 Techniques, 9, 2797-2812, 10.5194/amt-9-2797-2016, 2016.

910 Hedelius, J. K., He, T. L., Jones, D. B. A., Baier, B. C., Buchholz, R. R., De Mazière, M., Deutscher, N. M.,
911 Dubey, M. K., Feist, D. G., Griffith, D. W. T., Hase, F., Iraci, L. T., Jeseck, P., Kiel, M., Kivi, R., Liu, C.,
912 Morino, I., Notholt, J., Oh, Y. S., Ohyama, H., Pollard, D. F., Rettinger, M., Roche, S., Roehl, C. M.,
913 Schneider, M., Shiomi, K., Strong, K., Sussmann, R., Sweeney, C., Té, Y., Uchino, O., Velazco, V. A., Wang,
914 W., Warneke, T., Wennberg, P. O., Worden, H. M., and Wunch, D.: Evaluation of MOPITT Version 7 joint
915 TIR–NIR XCO retrievals with TCCON, Atmos. Meas. Tech., 12, 5547-5572, 10.5194/amt-12-5547-2019,
916 2019.

917   Ivatt, P. D., and Evans, M. J.: Improving the prediction of an atmospheric chemistry transport model
918   using gradient-boosted regression trees, Atmospheric Chemistry and Physics, 20, 8063-8082,
919   10.5194/acp-20-8063-2020, 2020.

920   Keller, C. A., and Evans, M. J.: Application of random forest regression to the calculation of gas-phase
921   chemistry within the GEOS-Chem chemistry model v10, Geoscientific Model Development, 12, 1209-
922   1225, 10.5194/gmd-12-1209-2019, 2019.

923   Kelp, M. M., Jacob, D. J., Kutz, J. N., Marshall, J. D., and Tessum, C. W.: Toward Stable, General Machine-
924   Learned Models of the Atmospheric Chemical System, Journal of Geophysical Research: Atmospheres,
925   125, e2020JD032759, https://doi.org/10.1029/2020JD032759, 2020.

926   Labow, G. J., McPeters, R. D., Bhartia, P. K., and Kramarova, N.: A comparison of 40 years of SBUV
927   measurements of column ozone with data from the Dobson/Brewer network, Journal of Geophysical
928   Research: Atmospheres, 118, 7370-7378, https://doi.org/10.1002/jgrd.50503, 2013.

929   Lamsal, L. N., Krotkov, N. A., Celarier, E. A., Swartz, W. H., Pickering, K. E., Bucsela, E. J., Gleason, J. F.,
930   Martin, R. V., Philip, S., Irie, H., Cede, A., Herman, J., Weinheimer, A., Szykman, J. J., and Knepp, T. N.:
931   Evaluation of OMI operational standard NO2 column retrievals using in situ and surface-based NO2
932   observations, Atmospheric Chemistry and Physics, 14, 11587-11609, 10.5194/acp-14-11587-2014, 2014.

933   Lamsal, L. N., Krotkov, N. A., Vasilkov, A., Marchenko, S., Qin, W., Yang, E. S., Fasnacht, Z., Joiner, J., Choi,
934   S., Haffner, D., Swartz, W. H., Fisher, B., and Bucsela, E.: Ozone Monitoring Instrument (OMI) Aura
935   nitrogen dioxide standard product version 4.0 with improved surface and cloud treatments, Atmos.
936   Meas. Tech., 14, 455-479, 10.5194/amt-14-455-2021, 2021.

937   Lamsal, L. N., Krotkov, N. A., Marchenko, S. V., Joiner, J., Oman, L., Vasilkov, A., Fisher, B., Qin, W., Yang,
938   E.-S., Fasnacht, Z., Choi, S., Leonard, P., and Haffner, D.: TROPOMI/S5P NO$_2$ Tropospheric, Stratospheric
939   and Total Columns MINDS 1-Orbit L2 Swath 5.5 km x 3.5 km, in, NASA Goddard Earth Sciences Data and
940   Information Services Center (GES DISC) [data set], https://10.5067/MEASURES/MINDS/Data203, 2022.

941   Laughner, J. L., Neu, J. L., Schimel, D., Wennberg, P. O., Barsanti, K., Bowman, K. W., Chatterjee, A.,
942   Croes, B. E., Fitzmaurice, H. L., Henze, D. K., Kim, J., Kort, E. A., Liu, Z., Miyazaki, K., Turner, A. J.,
943   Anenberg, S., Avise, J., Cao, H., Crisp, D., de Gouw, J., Eldering, A., Fyfe, J. C., Goldberg, D. L., Gurney, K.
944   R., Hasheminassab, S., Hopkins, F., Ivey, C. E., Jones, D. B. A., Liu, J., Lovenduski, N. S., Martin, R. V.,
945   McKinley, G. A., Ott, L., Poulter, B., Ru, M., Sander, S. P., Swart, N., Yung, Y. L., and Zeng, Z. C.: Societal
946   shifts due to COVID-19 reveal large-scale complexities and feedbacks between atmospheric chemistry
947   and climate change, Proc Natl Acad Sci U S A, 118, e2109481118, 10.1073/pnas.2109481118, 2021.

948   Lelieveld, J., Gromov, S., Pozzer, A., and Taraborrelli, D.: Global tropospheric hydroxyl distribution,
949   budget and reactivity, Atmos. Chem. Phys., 16, 12477-12493, 10.5194/acp-16-12477-2016, 2016.

950   Levy, R. C., Mattoo, S., Munchak, L. A., Remer, L. A., Sayer, A. M., Patadia, F., and Hsu, N. C.: The
951   Collection 6 MODIS aerosol products over land and ocean, Atmos. Meas. Tech., 6, 2989-3034,
952   10.5194/amt-6-2989-2013, 2013.

953   Liang, Q., Chipperfield, M. P., Fleming, E. L., Abraham, N. L., Braesicke, P., Burkholder, J. B., Daniel, J. S.,
954   Dhomse, S., Fraser, P. J., Hardiman, S. C., Jackman, C. H., Kinnison, D. E., Krummel, P. B., Montzka, S. A.,
955   Morgenstern, O., McCulloch, A., Mühle, J., Newman, P. A., Orkin, V. L., Pitari, G., Prinn, R. G., Rigby, M.,

956 Rozanov, E., Stenke, A., Tummon, F., Velders, G. J. M., Visioni, D., and Weiss, R. F.: Deriving Global OH
957 Abundance and Atmospheric Lifetimes for Long-Lived Gases: A Search for CH3CCl3 Alternatives, Journal
958 of Geophysical Research: Atmospheres, 122, 11,914-911,933, 10.1002/2017JD026926, 2017.

959 Lovelock, J. E.: Methyl chloroform in the troposphere as an indicator of OH radical abundance, Nature,
960 267, 32-32, 10.1038/267032a0, 1977.

961 Mao, J., Ren, X., Brune, W. H., Olson, J. R., Crawford, J. H., Fried, A., Huey, L. G., Cohen, R. C., Heikes, B.,
962 Singh, H. B., Blake, D. R., Sachse, G. W., Diskin, G. S., Hall, S. R., and Shetter, R. E.: Airborne measurement
963 of OH reactivity during INTEX-B, Atmos. Chem. Phys., 9, 163-173, 10.5194/acp-9-163-2009, 2009.

964 Martínez-Alonso, S., Deeter, M., Worden, H., Borsdorff, T., Aben, I., Commane, R., Daube, B., Francis, G.,
965 George, M., Landgraf, J., Mao, D., McKain, K., and Wofsy, S.: 1.5 years of TROPOMI CO measurements:
966 comparisons to MOPITT and ATom, Atmos. Meas. Tech., 13, 4841-4864, 10.5194/amt-13-4841-2020,
967 2020.

968 McPeters, R. D., Frith, S., and Labow, G. J.: OMI total column ozone: extending the long-term data
969 record, Atmos. Meas. Tech., 8, 4845-4850, 10.5194/amt-8-4845-2015, 2015.

970 Miller, D. O., and Brune, W. H.: Investigating the Understanding of Oxidation Chemistry Using 20 Years
971 of Airborne OH and HO2 Observations, Journal of Geophysical Research: Atmospheres, 127,
972 e2021JD035368, https://doi.org/10.1029/2021JD035368, 2022.

973 Miyazaki, K., Bowman, K. W., Yumimoto, K., Walker, T., and Sudo, K.: Evaluation of a multi-model, multi-
974 constituent assimilation framework for tropospheric chemical reanalysis, Atmos. Chem. Phys., 20, 931-
975 967, 10.5194/acp-20-931-2020, 2020.

976 Miyazaki, K., Bowman, K., Sekiya, T., Takigawa, M., Neu, J. L., Sudo, K., Osterman, G., and Eskes, H.:
977 Global tropospheric ozone responses to reduced NOx emissions linked to the COVID-19 worldwide
978 lockdowns, Science Advances, 7, eabf7460, 10.1126/sciadv.abf7460, 2021.

979 Montzka, S. A., Krol, M., Dlugokencky, E., Hall, B., Jockel, P., and Lelieveld, J.: Small Interannual
980 Variability of Global Atmospheric Hydroxyl, Science, 331, 67-69, 10.1126/science.1197640, 2011.

981 Murray, L. T., Mickley, L. J., Kaplan, J. O., Sofen, E. D., Pfeiffer, M., and Alexander, B.: Factors controlling
982 variability in the oxidative capacity of the troposphere since the Last Glacial Maximum, Atmospheric
983 Chemistry and Physics, 14, 3589-3622, 10.5194/acp-14-3589-2014, 2014.

984 Murray, L. T., Fiore, A. M., Shindell, D. T., Naik, V., and Horowitz, L. W.: Large uncertainties in global
985 hydroxyl projections tied to fate of reactive nitrogen and carbon, Proceedings of the National Academy
986 of Sciences, 118, e2115204118, 10.1073/pnas.2115204118, 2021.

987 NASA Goddard Space Flight Center. MERRA2 GMI, NASA [data set], https://acd-
988 ext.gsfc.nasa.gov/Projects/GEOSCCM/MERRA2GMI/, last access: 6 March 2023.

989 Nault, B. A., Garland, C., Pusede, S. E., Wooldridge, P. J., Ullmann, K., Hall, S. R., and Cohen, R. C.:
990 Measurements of $CH_3O_2NO_2$ in the upper troposphere, Atmospheric Measurement Techniques, 8, 987-
991 997, 10.5194/amt-8-987-2015, 2015.

Naus, S., Montzka, S. A., Pandey, S., Basu, S., Dlugokencky, E. J., and Krol, M.: Constraints and biases in a tropospheric two-box model of OH, Atmos. Chem. Phys., 19, 407-424, 10.5194/acp-19-407-2019, 2019.

Naus, S., Montzka, S. A., Patra, P. K., and Krol, M. C.: A three-dimensional-model inversion of methyl chloroform to constrain the atmospheric oxidative capacity, Atmospheric Chemistry and Physics, 21, 4809-4824, 10.5194/acp-21-4809-2021, 2021.

Nicely, J. M., Salawitch, R. J., Canty, T., Anderson, D. C., Arnold, S. R., Chipperfield, M. P., Emmons, L. K., Flemming, J., Huijnen, V., Kinnison, D. E., Lamarque, J.-F., Mao, J., Monks, S. A., Steenrod, S. D., Tilmes, S., and Turquety, S.: Quantifying the causes of differences in tropospheric OH within global models, Journal of Geophysical Research: Atmospheres, JD026239, 10.1002/2016JD026239, 2017.

Nicely, J. M., Duncan, B. N., Hanisco, T. F., Wolfe, G. M., Salawitch, R. J., Deushi, M., Haslerud, A. S., Jöckel, P., Josse, B., Kinnison, D. E., Klekociuk, A., Manyin, M. E., Marécal, V., Morgenstern, O., Murray, L. T., Myhre, G., Oman, L. D., Pitari, G., Pozzer, A., Quaglia, I., Revell, L. E., Rozanov, E., Stenke, A., Stone, K., Strahan, S., Tilmes, S., Tost, H., Westervelt, D. M., and Zeng, G.: A machine learning examination of hydroxyl radical differences among model simulations for CCMI-1, Atmospheric Chemistry and Physics, 20, 1341-1361, 10.5194/acp-20-1341-2020, 2020.

Oman, L. D., Douglass, A. R., Ziemke, J. R., Rodriguez, J. M., Waugh, D. W., and Nielsen, J. E.: The ozone response to ENSO in Aura satellite measurements and a chemistry-climate simulation, Journal of Geophysical Research-Atmospheres, 118, 965-976, 10.1029/2012jd018546, 2013.

Orbe, C., Oman, L. D., Strahan, S. E., Waugh, D. W., Pawson, S., Takacs, L. L., and Molod, A. M.: Large-Scale Atmospheric Transport in GEOS Replay Simulations, Journal of Advances in Modeling Earth Systems, 9, 2545-2560, 10.1002/2017ms001053, 2017.

Patra, P. K., Krol, M. C., Montzka, S. A., Arnold, T., Atlas, E. L., Lintner, B. R., Stephens, B. B., Xiang, B., Elkins, J. W., Fraser, P. J., Ghosh, A., Hintsa, E. J., Hurst, D. F., Ishijima, K., Krummel, P. B., Miller, B. R., Miyazaki, K., Moore, F. L., Muhle, J., O'Doherty, S., Prinn, R. G., Steele, L. P., Takigawa, M., Wang, H. J., Weiss, R. F., Wofsy, S. C., and Young, D.: Observational evidence for interhemispheric hydroxyl-radical parity, Nature, 513, 219-223, 10.1038/nature13721, 2014.

Pérez-Ramírez, D., Smirnov, A., Pinker, R. T., Petrenko, M., Román, R., Chen, W., Ichoku, C., Noël, S., Abad, G. G., Lyamani, H., and Holben, B. N.: Precipitable water vapor over oceans from the Maritime Aerosol Network: Evaluation of global models and satellite products under clear sky conditions, Atmospheric Research, 215, 294-304, https://doi.org/10.1016/j.atmosres.2018.09.007, 2019.

Pickett, H. M., Drouin, B. J., Canty, T., Salawitch, R. J., Fuller, R. A., Perun, V. S., Livesey, N. J., Waters, J. W., Stachnik, R. A., Sander, S. P., Traub, W. A., Jucks, K. W., and Minschwaner, K.: Validation of Aura Microwave Limb Sounder OH and HO_2 measurements, Journal of Geophysical Research: Atmospheres, 113, D16S30, https://doi.org/10.1029/2007JD008775, 2008.

Pimlott, M. A., Pope, R. J., Kerridge, B. J., Latter, B. G., Knappett, D. S., Heard, D. E., Ventress, L. J., Siddans, R., Feng, W., and Chipperfield, M. P.: Investigating the global OH radical distribution using steady-state approximations and satellite data, Atmos. Chem. Phys., 22, 10467-10488, 10.5194/acp-22-10467-2022, 2022.

1030 Rigby, M., Montzka, S. A., Prinn, R. G., White, J. W. C., Young, D., O'Doherty, S., Lunt, M. F., Ganesan, A.
1031 L., Manning, A. J., Simmonds, P. G., Salameh, P. K., Harth, C. M., Muhle, J., Weiss, R. F., Fraser, P. J.,
1032 Steele, L. P., Krummel, P. B., McCulloch, A., and Park, S.: Role of atmospheric oxidation in recent
1033 methane growth, Proc Natl Acad Sci U S A, 114, 5373-5377, 10.1073/pnas.1616426114, 2017.

1034 Shah, V., Jacob, D. J., Dang, R., Lamsal, L. N., Strode, S. A., Steenrod, S. D., Boersma, K. F., Eastham, S. D.,
1035 Fritz, T. M., Thompson, C., Peischl, J., Bourgeois, I., Pollack, I. B., Nault, B. A., Cohen, R. C., Campuzano-
1036 Jost, P., Jimenez, J. L., Andersen, S. T., Carpenter, L. J., Sherwen, T., and Evans, M. J.: Nitrogen oxides in
1037 the free troposphere: implications for tropospheric oxidants and the interpretation of satellite NO_2
1038 measurements, Atmos. Chem. Phys., 23, 1227-1257, 10.5194/acp-23-1227-2023, 2023.

1039 Silvern, R. F., Jacob, D. J., Travis, K. R., Sherwen, T., Evans, M. J., Cohen, R. C., Laughner, J. L., Hall, S. R.,
1040 Ullmann, K., Crounse, J. D., Wennberg, P. O., Peischl, J., and Pollack, I. B.: Observed NO/NO2 Ratios in
1041 the Upper Troposphere Imply Errors in $NO-NO_2-O_3$ Cycling Kinetics or an Unaccounted NOx Reservoir,
1042 Geophysical Research Letters, 45, 4466-4474, https://doi.org/10.1029/2018GL077728, 2018.

1043 Spivakovsky, C. M., Yevich, R., Logan, J. A., Wofsy, S. C., McElroy, M. B., and Prather, M. J.: Tropospheric
1044 OH in a three-dimensional chemical tracer model: An assessment based on observations of CH_3CCl_3,
1045 Journal of Geophysical Research: Atmospheres, 95, 18441-18471, 10.1029/JD095iD11p18441, 1990.

1046 Stauffer, R. M., Thompson, A. M., and Young, G. S.: Tropospheric ozonesonde profiles at long-term U.S.
1047 monitoring sites: 1. A climatology based on self-organizing maps, Journal of Geophysical Research:
1048 Atmospheres, 121, 1320-1339, https://doi.org/10.1002/2015JD023641, 2016.

1049 Stevenson, D. S., Zhao, A., Naik, V., amp, apos, Connor, F. M., Tilmes, S., Zeng, G., Murray, L. T., Collins,
1050 W. J., Griffiths, P., Shim, S., Horowitz, L. W., Sentman, L., and Emmons, L.: Trends in global tropospheric
1051 hydroxyl radical and methane lifetime since 1850 from AerChemMIP, Atmos. Chem. Phys., 20, 12905-
1052 12920, https://doi.org/10.5194/acp-20-12905-2020, 2020.

1053
1054 Strahan, S. E., Duncan, B. N., and Hoor, P.: Observationally derived transport diagnostics for the
1055 lowermost stratosphere and their application to the GMI chemistry and transport model, Atmos. Chem.
1056 Phys., 7, 2435-2445, 10.5194/acp-7-2435-2007, 2007.

1057 Strode, S. A., Ziemke, J. R., Oman, L. D., Lamsal, L. N., Olsen, M. A., and Liu, J.: Global changes in the
1058 diurnal cycle of surface ozone, Atmospheric Environment, 199, 323-333,
1059 10.1016/j.atmosenv.2018.11.028, 2019.

1060 Susskind, J., Blaisdell, J. M., and Iredell, L.: Improved methodology for surface and atmospheric
1061 soundings, error estimates, and quality control procedures: the atmospheric infrared sounder science
1062 team version-6 retrieval algorithm, Journal of Applied Remote Sensing, 8, 084994,
1063 10.1117/1.Jrs.8.084994, 2014.

1064 Thompson, C. R., Wofsy, S. C., Prather, M. J., Newman, P. A., Hanisco, T. F., Ryerson, T. B., Fahey, D. W.,
1065 Apel, E. C., Brock, C. A., Brune, W. H., Froyd, K., Katich, J. M., Nicely, J. M., Peischl, J., Ray, E., Veres, P. R.,
1066 Wang, S., Allen, H. M., Asher, E., Bian, H., Blake, D., Bourgeois, I., Budney, J., Bui, T. P., Butler, A.,
1067 Campuzano-Jost, P., Chang, C., Chin, M., Commane, R., Correa, G., Crounse, J. D., Daube, B., Dibb, J. E.,
1068 DiGangi, J. P., Diskin, G. S., Dollner, M., Elkins, J. W., Fiore, A. M., Flynn, C. M., Guo, H., Hall, S. R.,
1069 Hannun, R. A., Hills, A., Hintsa, E. J., Hodzic, A., Hornbrook, R. S., Huey, L. G., Jimenez, J. L., Keeling, R. F.,
1070 Kim, M. J., Kupc, A., Lacey, F., Lait, L. R., Lamarque, J.-F., Liu, J., McKain, K., Meinardi, S., Miller, D. O.,

1071   Montzka, S. A., Moore, F. L., Morgan, E. J., Murphy, D. M., Murray, L. T., Nault, B. A., Neuman, J. A.,
1072   Nguyen, L., Gonzalez, Y., Rollins, A., Rosenlof, K., Sargent, M., Schill, G., Schwarz, J. P., Clair, J. M. S.,
1073   Steenrod, S. D., Stephens, B. B., Strahan, S. E., Strode, S. A., Sweeney, C., Thames, A. B., Ullmann, K.,
1074   Wagner, N., Weber, R., Weinzierl, B., Wennberg, P. O., Williamson, C. J., Wolfe, G. M., and Zeng, L.: The
1075   NASA Atmospheric Tomography (ATom) Mission: Imaging the Chemistry of the Global Atmosphere,
1076   Bulletin of the American Meteorological Society, 103, E761-E790, 10.1175/BAMS-D-20-0315.1, 2022.

1077   Turner, A. J., Frankenberg, C., Wennberg, P. O., and Jacob, D. J.: Ambiguity in the causes for decadal
1078   trends in atmospheric methane and hydroxyl, Proceedings of the National Academy of Sciences, 114,
1079   5367, 10.1073/pnas.1616020114, 2017.

1080   Turner, A. J., Fung, I., Naik, V., Horowitz, L. W., and Cohen, R. C.: Modulation of hydroxyl variability by
1081   ENSO in the absence of external forcing, Proc Natl Acad Sci U S A, 115, 8931-8936,
1082   10.1073/pnas.1807532115, 2018.

1083   van Geffen, J., Boersma, K. F., Eskes, H., Sneep, M., ter Linden, M., Zara, M., and Veefkind, J. P.: S5P
1084   TROPOMI NO2 slant column retrieval: method, stability, uncertainties and comparisons with OMI,
1085   Atmos. Meas. Tech., 13, 1315-1335, 10.5194/amt-13-1315-2020, 2020.

1086   Veefkind, J. P., Aben, I., McMullan, K., Förster, H., de Vries, J., Otter, G., Claas, J., Eskes, H. J., de Haan, J.
1087   F., Kleipool, Q., van Weele, M., Hasekamp, O., Hoogeveen, R., Landgraf, J., Snel, R., Tol, P., Ingmann, P.,
1088   Voors, R., Kruizinga, B., Vink, R., Visser, H., and Levelt, P. F.: TROPOMI on the ESA Sentinel-5 Precursor: A
1089   GMES mission for global observations of the atmospheric composition for climate, air quality and ozone
1090   layer applications, Remote Sensing of Environment, 120, 70-83,
1091   https://doi.org/10.1016/j.rse.2011.09.027, 2012.

1092   Verhoelst, T., Compernolle, S., Pinardi, G., Lambert, J. C., Eskes, H. J., Eichmann, K. U., Fjæraa, A. M.,
1093   Granville, J., Niemeijer, S., Cede, A., Tiefengraber, M., Hendrick, F., Pazmiño, A., Bais, A., Bazureau, A.,
1094   Boersma, K. F., Bognar, K., Dehn, A., Donner, S., Elokhov, A., Gebetsberger, M., Goutail, F., Grutter de la
1095   Mora, M., Gruzdev, A., Gratsea, M., Hansen, G. H., Irie, H., Jepsen, N., Kanaya, Y., Karagkiozidis, D., Kivi,
1096   R., Kreher, K., Levelt, P. F., Liu, C., Müller, M., Navarro Comas, M., Piters, A. J. M., Pommereau, J. P.,
1097   Portafaix, T., Prados-Roman, C., Puentedura, O., Querel, R., Remmers, J., Richter, A., Rimmer, J., Rivera
1098   Cárdenas, C., Saavedra de Miguel, L., Sinyakov, V. P., Stremme, W., Strong, K., Van Roozendael, M.,
1099   Veefkind, J. P., Wagner, T., Wittrock, F., Yela González, M., and Zehner, C.: Ground-based validation of
1100   the Copernicus Sentinel-5P TROPOMI NO$_2$ measurements with the NDACC ZSL-DOAS, MAX-DOAS and
1101   Pandonia global networks, Atmos. Meas. Tech., 14, 481-510, 10.5194/amt-14-481-2021, 2021.

1102   Voulgarakis, A., Naik, V., Lamarque, J. F., Shindell, D. T., Young, P. J., Prather, M. J., Wild, O., Field, R. D.,
1103   Bergmann, D., Cameron-Smith, P., Cionni, I., Collins, W. J., Dalsøren, S. B., Doherty, R. M., Eyring, V.,
1104   Faluvegi, G., Folberth, G. A., Horowitz, L. W., Josse, B., MacKenzie, I. A., Nagashima, T., Plummer, D. A.,
1105   Righi, M., Rumbold, S. T., Stevenson, D. S., Strode, S. A., Sudo, K., Szopa, S., and Zeng, G.: Analysis of
1106   present day and future OH and methane lifetime in the ACCMIP simulations, Atmospheric Chemistry and
1107   Physics, 13, 2563-2587, 10.5194/acp-13-2563-2013, 2013.

1108   Wang, P., Piters, A., van Geffen, J., Tuinder, O., Stammes, P., and Kinne, S.: Shipborne MAX-DOAS
1109   measurements for validation of TROPOMI NO$_2$ products, Atmos. Meas. Tech., 13, 1413-1426,
1110   10.5194/amt-13-1413-2020, 2020.

1111   Wells, K. C., Millet, D. B., Payne, V. H., Deventer, M. J., Bates, K. H., de Gouw, J. A., Graus, M., Warneke,
1112   C., Wisthaler, A., and Fuentes, J. D.: Satellite isoprene retrievals constrain emissions and atmospheric
1113   oxidation, Nature, 585, 225-233, 10.1038/s41586-020-2664-3, 2020.

1114   Wild, O., Voulgarakis, A., amp, apos, Connor, F., Lamarque, J.-F., Ryan, E. M., and Lee, L.: Global
1115   sensitivity analysis of chemistry-climate model budgets of tropospheric ozone and OH: exploring model
1116   diversity, Atmospheric Chemistry and Physics, 20, 4047-4058, 10.5194/acp-20-4047-2020, 2020.

1117   Wolfe, G. M., Nicely, J. M., St Clair, J. M., Hanisco, T. F., Liao, J., Oman, L. D., Brune, W. B., Miller, D.,
1118   Thames, A., Gonzalez Abad, G., Ryerson, T. B., Thompson, C. R., Peischl, J., McCain, K., Sweeney, C.,
1119   Wennberg, P. O., Kim, M., Crounse, J. D., Hall, S. R., Ullmann, K., Diskin, G., Bui, P., Chang, C., and Dean-
1120   Day, J.: Mapping hydroxyl variability throughout the global remote troposphere via synthesis of airborne
1121   and satellite formaldehyde observations, Proc Natl Acad Sci U S A, 116, 11171-11180,
1122   10.1073/pnas.1821661116, 2019.

1123   Wolter, K., and Timlin, M. S.: El Niño/Southern Oscillation behaviour since 1871 as diagnosed in an
1124   extended multivariate ENSO index (MEI.ext), International Journal of Climatology, 31, 1074-1087,
1125   10.1002/joc.2336, 2011.

1126   Zhao, Y., Saunois, M., Bousquet, P., Lin, X., Berchet, A., Hegglin, M. I., Canadell, J. G., Jackson, R. B.,
1127   Hauglustaine, D. A., Szopa, S., Stavert, A. R., Abraham, N. L., Archibald, A. T., Bekki, S., Deushi, M., Jöckel,
1128   P., Josse, B., Kinnison, D., Kirner, O., Marécal, V., Connor, F. M., Plummer, D. A., Revell, L. E., Rozanov, E.,
1129   Stenke, A., Strode, S., Tilmes, S., Dlugokencky, E. J., and Zheng, B.: Inter-model comparison of global
1130   hydroxyl radical (OH) distributions and their impact on atmospheric methane over the 2000-2016
1131   period, Atmospheric Chemistry and Physics, 19, 13701-13723, 10.5194/acp-19-13701-2019, 2019.

1132   Zhu, L., Jacob, D. J., Kim, P. S., Fisher, J. A., Yu, K., Travis, K. R., Mickley, L. J., Yantosca, R. M., Sulprizio, M.
1133   P., De Smedt, I., González Abad, G., Chance, K., Li, C., Ferrare, R., Fried, A., Hair, J. W., Hanisco, T. F.,
1134   Richter, D., Jo Scarino, A., Walega, J., Weibring, P., and Wolfe, G. M.: Observing atmospheric
1135   formaldehyde (HCHO) from space: validation and intercomparison of six retrievals from four satellites
1136   (OMI, GOME2A, GOME2B, OMPS) with SEAC^{4}RS aircraft observations over the southeast US,
1137   Atmospheric Chemistry and Physics, 16, 13477-13490, 10.5194/acp-16-13477-2016, 2016.
1138
1139   Zhu, Q., Laughner, J. L., and Cohen, R. C.: Estimate of OH trends over one decade in North American
1140   cities, Proc Natl Acad Sci U S A, 119, e2117399119, https://doi.org/10.1073/pnas.2117399119, 2022a.

1141   Zhu, Q., Laughner, J. L., and Cohen, R. C.: Combining Machine Learning and Satellite Observations to
1142   Predict Spatial and Temporal Variation of near Surface OH in North American Cities, Environmental
1143   Science & Technology, 7362 - 7371, 10.1021/acs.est.1c05636, 2022b.
1144